

EMFusion: Conditional Diffusion Framework for Trustworthy Frequency Selective EMF Forecasting in Wireless Networks

Zijiang Yan*[✉], Yixiang Huang*[✉], Jianhua Pei[✉], *Graduate Student Member, IEEE*,
Hina Tabassum[✉], *Senior Member, IEEE*, and Luca Chiaravaglio[✉], *Senior Member, IEEE*

Abstract—The rapid growth in wireless infrastructure has increased the need to accurately estimate and forecast electromagnetic field (EMF) levels to ensure ongoing compliance, assess potential health impacts, and support efficient network planning. While existing studies rely on univariate forecasting of wideband aggregate EMF data, frequency-selective multivariate forecasting is needed to capture the inter-operator and inter-frequency variations essential for proactive network planning. To this end, this paper introduces EMFusion, a conditional multivariate diffusion-based probabilistic forecasting framework that integrates diverse contextual factors (e.g., time of day, season, and holidays) while providing explicit uncertainty estimates. The proposed architecture features a residual U-Net backbone enhanced by a cross-attention mechanism that dynamically integrates external conditions to guide the generation process. Furthermore, EMFusion integrates an imputation-based sampling strategy that treats forecasting as a structural inpainting task, ensuring temporal coherence even with irregular measurements. Unlike standard point forecasters, EMFusion generates calibrated probabilistic prediction intervals directly from the learned conditional distribution, providing explicit uncertainty quantification essential for trustworthy decision-making. Numerical experiments conducted on frequency-selective EMF datasets demonstrate that EMFusion with the contextual information of working hours outperforms the baseline models with or without conditions. The EMFusion outperforms the best baseline by 23.85% in continuous ranked probability score (CRPS), 13.93% in normalized root mean square error, and reduces prediction CRPS error by 22.47%.

Index Terms—Electromagnetic field (EMF), EMF exposure forecasting, conditional diffusion model, probabilistic forecasting, uncertainty quantification, wireless communication network.

I. INTRODUCTION

The rapid proliferation of new wireless communication technologies, such as transmissions at higher frequencies, massive antennas, and reconfigurable intelligent surfaces, has led to an unprecedented increase in the radio-frequency (RF)-based electromagnetic field (EMF) sources [1], [2]. This technological surge has amplified public and regulatory concerns regarding potential human health effects associated with EMF exposure [2], [3]. Consequently, accurate EMF monitoring and

Z. Yan and H. Tabassum are with the department of Electrical Engineering and Computer Science, York University, Toronto, Canada (e-mails: {zijiang, hinat}@yorku.ca). Y. Huang and J. Pei are with the School of Electrical and Electronic Engineering, Huazhong University of Science and Technology, Wuhan, China (e-mails: yxhuang@hust.edu.cn, jianhuapei98@gmail.com). J. Pei is also with the Central China Branch of State Grid Corporation of China, Wuhan, China. L. Chiaravaglio is with the Department of Electronic Engineering, University of Rome Tor Vergata, Rome, Italy (e-mail: luca.chiaravaglio@uniroma2.it). L. Chiaravaglio is also with the Consorzio Nazionale Interuniversitario per le Telecomunicazioni (CNIT), Parma, Italy. Z. Yan and Y. Huang contributed equally to this work and are co-first authors.

forecasting is becoming indispensable for regulatory compliance and for optimizing network deployment and resource management in a proactive manner [1], [4].

To date, existing research studies in the domain focused on univariate forecasting of aggregate EMF exposure collected across a large bandwidth [1]. However, knowing the wideband EMF exposure is often not enough for active network planning or proactive network resource allocation. Instead a detailed frequency selective EMF exposure breakdown is necessary to identify dominant exposure sources and pin-point the EMF contributions from specific technologies (e.g., 3G, 4G, and 5G deployments) and network operators. Frequency selective EMF forecasting enables regulatory compliance with higher granularity, optimize network deployment as well as spectrum and power allocation policies. Nevertheless, due to the scarcity of frequency selective EMF datasets, forecasting EMF contributions at specific transmission frequencies with multiple network operators and/or diverse wireless technologies remain a fundamental challenge.

Along another note, the uncertainty in EMF patterns, driven by fluctuating network traffic, user mobility, and propagation conditions, means that deterministic point forecasts are insufficient due to the significant errors they produce. Probabilistic forecasting approaches can provide a comprehensive understanding of potential EMF exposure levels, including their likelihood, range, and associated uncertainties [5].

Over the past decade, deep learning (DL) solutions have achieved remarkable progress in time-series forecasting (TSF), yet the trained models remain limited in their ability to represent uncertainty and complex temporal dynamics. Conventional architectures such as recurrent neural networks (RNNs) and transformers are primarily designed for deterministic prediction, producing single-point forecasts that often overlook the inherent randomness of real-world systems. As a result, these models can yield overconfident estimates and struggle to generalize under noisy, incomplete, or dynamic conditions. Moreover, their autoregressive nature can lead to error accumulation over extended horizons, reducing long-term reliability. Recently, Generative diffusion models (DMs) enable learning the full probability distribution of future trajectories through an iterative denoising process [5]–[7]. This approach enables them to generate diverse and realistic forecasts, impute missing or corrupted data, transmit semantic wireless signals with high fidelity [8], [9], and flexibly incorporate contextual variables such as seasonal, holiday, or working hour trends [10]. By combining probabilistic reasoning with stable and interpretable generation, diffusion-based forecasting represents a significant step forward in capturing the uncertainty and

complexity of temporal phenomena.

To this end, this paper proposes *EMFusion*, a conditional diffusion model (CDM) for multivariate probabilistic forecasting of EMF exposure at different frequencies. The considered frequency-selective EMF datasets are multivariate since each timestamp contains a set of EMF measurements across multiple frequency bands, wireless technologies, and network operators, forming a multidimensional observation vector. Modeling these jointly, rather than independently, enables capturing interdependencies such as shared temporal patterns, correlated behavior, and coupled exposure dynamics. As such, *EMFusion* is capable to model the joint distribution of multi-frequency EMF exposure trajectories, capture complex inter-frequency dependencies, and provide built-in uncertainty quantification directly from the generative process, eliminating the need for post-hoc calibration wrappers. To our best knowledge, none of the existing research in the domain of wireless networks have applied conditional DMs for TSF in general and for EMF TSF in particular. The specific contributions of this paper can thus be summarized as follows:

- 1) The proposed *EMFusion* is based on a CDM for multivariate probabilistic forecasting of frequency-specific EMF exposure that allows the generation process to be guided by various contextual factors or conditions. *EMFusion* leverages contextual variables such as time of the day, day of the week, holiday/working days, working hours, and seasonal trends. This conditioning not only enhances the accuracy and relevance of the forecasts, but also allows for the generation of scenarios tailored to specific environmental states. The proposed architecture features a residual U-Net backbone enhanced by a cross-attention mechanism that dynamically integrates external conditions to guide the generation process. Furthermore, *EMFusion* integrates an imputation-based sampling strategy that treats forecasting as a structural inpainting task, ensuring temporal coherence even with irregular or missing EMF measurements.
- 2) Unlike conventional point forecasters that output a single trajectory, we propose a robust interval estimation framework based on the generative capabilities of *EMFusion*. By treating the ensemble of generated trajectories as samples from a conditional distribution, we employ Kernel Density Estimation (KDE) to reconstruct continuous probability density functions at each time step. This approach enables the derivation of empirically calibrated prediction intervals without imposing parametric Gaussian assumptions, thereby achieving empirically validated coverage at prescribed confidence levels and providing trustworthy uncertainty quantification on EMF multivariate forecasting rather than simple point estimation.
- 3) *EMFusion* can be customized for both univariate and multivariate forecasting scenarios. Multivariate forecasting captures correlation across distinct network operators, transmission frequencies, and wireless technologies. Meanwhile, a univariate approach remains beneficial for scenarios where data or computational resources are limited, enabling fast, frequency-specific forecasts that

are simpler to implement for localized optimization.

- 4) We conduct experiments on frequency-selective EMF exposure datasets spanning multiple narrowband channels in the frequency range of 9 kHz–6 GHz, thus covering major network operators in the Italy and cellular network technologies. Numerical results confirm the effectiveness of the conditional over unconditional *EMFusion*, and multivariate over univariate *EMFusion*. Among various exogenous conditions, we note that the working hour condition outperforms. Furthermore, the *EMFusion* outperforms the best baseline by around 23.85% continuous ranked probability score (CRPS), 13.93% normalized root mean square error (NRMSE) and reduces prediction CRPS error by 22.47%.

The remainder of this paper is organized as follows. Section II presents the existing state-of-the-art for TSF in wireless networks. Section III presents the architecture of the proposed multivariate *EMFusion* model. The experimental setup, data analysis, and visualizations are presented in Section IV followed by numerical results and discussions in Section V. Finally, Section VI concludes the paper.

II. RELATED WORK

TSF for wireless networks has evolved from classical statistical techniques to DL and, most recently, to generative AI. This subsection provides a review of existing state-of-the-art techniques for TSF and EMF forecasting in wireless networks.

1) *Statistical Methods for TSF*: Initial approaches to EMF exposure forecasting relied on classical time-series models. These included autoregressive models like ARIMA [27], as well as methods such as kernel ridge regression and support-vector regression. While computationally lightweight and interpretable, these techniques often assume stationarity and require significant manual feature engineering. Their linear parametrization also limits their accuracy when the underlying drivers of EMF exposure interact non-linearly across multiple time scales. A representative approach is found in [28], who proposed a model that decomposes wide-band EMF radiation into three distinct components: the average exposure level, daily and half-daily periodic patterns (seasonal behavior), and the temporal correlation among residuals [28]. Their model effectively captured different behaviors between weekdays and weekends by applying separate autoregressive model for weekdays and Sunday, and the other autoregressive model for Saturday [28]. While effective, such methods are tailored to specific observed periodicities and struggle to generalize without manual recalibration.

2) *Deep Learning for TSF*: In this subsection, we classify DL approaches for TSF in wireless networks, including network traffic forecasting, QoS prediction, channel prediction, and EMF forecasting.

a) *Network Traffic Forecasting*: [11] compared Multi-Layer Perceptrons (MLP) as well as Support Vector Machines (SVM), to predict traffic in commercial Long-Term Evolution (LTE) networks. Similarly, [13] developed a univariate forecasting platform for 4G networks using Long Short-Term Memory (LSTM) and Recurrent Neural Networks

TABLE I: Classification of deep learning models for wireless networks forecasting/prediction applications. **UV**: Univariate forecasting; **MV**: Multivariate forecasting; **Cond.**: External Conditions; **Imp.**: Imputation; **Trust.**: Trustworthiness.

Domain	Ref.	Model	Target Dataset	UV/MV	Cond.	Imp.	Trust.
Network Traffic	[11]	MLP, MLPWD, SVM	Commercial LTE trial traffic	UV/MV	—	—	—
	[12]	VAR, RNN	LTE-A VoIP traffic	UV/MV	—	—	—
	[13]	LSTM RNN	Vodafone 4G throughput	UV	—	—	—
	[14]	Transformer	5G/LTE O-RAN aggregate traffic	UV	—	—	—
	[15]	LSTM + XAI	4G load and active-user datasets	UV	—	—	—
Channel Prediction	[16]	VAR, LSTM	ubiquitous healthcare traffic	MV	—	—	—
	[17]	Holt-Winters, LSTM	Real enterprise WLAN traffic	UV/MV	BS Traffic	—	—
	[18]	LSTM (SCP), RNN	Synthetic LEO mMIMO CSI	UV	—	—	—
QoS Prediction	[19]	Temporal Transformer	Real IoT smart-building datasets	UV/MV	—	✓	—
	[20]	BiLSTM-CNN	CDN video streaming QoE dataset	MV	—	—	—
	[21]	LSTM, Seq2Seq	Rural fixed-wireless LTE KPIs	MV	Weather	✓	—
	[22]	Diffusion + TCN	Real DTN-inspired sensor datasets	MV	Tempreature	—	✓
EMF Exposure	[23]	k-NN, XGBoost	EMF measurements	UV	Population Density	—	XAI
	[24]	CNN	Wideband RF-EMF	UV	—	—	—
	[25]	LSTM, RNN	Wideband RF-EMF	UV	—	—	—
	[26]	Transformer, CNN	Wideband RF-EMF	MV	—	—	—
	[1]	Patching, MLP	Wideband RF-EMF	UV	—	—	✓
EMFusion	CDM + Cross attention	Frequency Selective RF-EMF	UV/MV	Time, Date, Season	✓	✓	

(RNNs), demonstrating superiority over statistical baselines like ARIMA. More recent studies have shifted toward multivariate and interpretable models. [12] characterized LTE-Advanced Voice-over-IP metrics using Vector Autoregression (VAR) and supervised DL sliding-window frameworks. To enhance interpretability, [15] introduced AICHRONOLENS, an Explainable AI (XAI) framework that correlates temporal structures with LSTM error diagnoses. In the context of Software-Defined Networking, [16] utilized LSTM to model jointly evolving traffic flows for healthcare applications. Furthermore, for open radio access networks, [14] proposed a Transformer-based Autoformer architecture to predict aggregate cell traffic. While these methods achieve strong deterministic accuracy, they primarily focus on point forecasting. They generally lack explicit mechanisms for data imputation handling missing values and do not provide intrinsic uncertainty quantification essential for trustworthy network planning.

b) *Channel Prediction*: Channel prediction is critical for mitigating aging in high-mobility scenarios. [17] benchmarked various models, including Holt-Winters and XGBoost, against LSTMs for enterprise Wireless Local Area Network traffic, analyzing spatio-temporal Access Point (AP) clustering. In satellite communications, [18] proposed a Satellite Channel Predictor based on LSTM units for Low Earth Orbit (LEO) massive Multiple-Input Multiple-Output (mMIMO) systems. Their approach outperformed Kalman filters and standard RNNs in multi-step Channel State Information (CSI) forecasting. Similar to traffic forecasting, these works rely on deterministic models and do not account for the confidence level of predictions, which is vital for robust resource allocation.

c) *Quality of Service (QoS) Prediction*: Forecasting QoS involves modeling complex dependencies. [20] introduced

a hybrid bidirectional LSTM (BiLSTM) and Convolutional neural network (CNN) architecture for multivariate QoS forecasting in Content Delivery Networks (CDNs). [19] utilized a temporal Transformer encoder to predict QoS metrics in IoT networks, effectively capturing long-term dependencies that RNNs often miss. [21] investigated Sequence-to-Sequence (Seq2Seq) models for rural LTE Key Performance Indicators (KPIs), noting that exogenous features provided minimal gains due to short temporal dependencies.

d) *EMF Exposure Forecasting*: Research in EMF forecasting has progressed from spatial regression to time-series analysis. [23] focused on comparative regression using ensemble methods like Random Forest to rank urban factors affecting EMF levels. For temporal forecasting, [25] demonstrated that LSTMs outperform classical statistical models (e.g., ARIMA) in long-term (over a 60-month period) for univariate EMF prediction. Recently, [26] demonstrated the effectiveness of 1-D CNNs in handling single-step and multi-step EMF forecasting tasks by leveraging translation invariance to identify periodicities in the data. Other research works also adapted CNN designs, utilizing architectures like Radial Basis Function Networks and Generalized Regression Neural Networks to model complex RF-EMF signals from emerging technologies like 5G [29]. Despite the aforementioned advancements, significant research gaps remain in the domain.

- 1) Existing EMF studies rely on univariate forecasting of aggregate EMF levels collected over a large bandwidth. Thus, they fail to capture the inter-operator and inter-frequency correlations essential for network planning.
- 2) Approaches like [1] rely on post-hoc calibration rather than learning the joint probability distribution directly.

This decoupling can limit the expressiveness of the uncertainty representation. To address this, recent work has turned to distribution-free methods like conformal prediction. A notable example is EMFORECASTER [1], which integrates a powerful PatchTST backbone with a post-hoc conformal calibration layer. This two-stage pipeline delivers statistically valid prediction intervals for EMF levels. However, by decoupling uncertainty quantification from the primary sequence modeling, this approach is not directly applicable to multivariate frequency selective forecasting that adhere to the physical constraints and interdependencies across different frequency carriers, wireless technologies, and operators. Furthermore, EMFORECASTER [1] is designed for univariate forecasting, thus a large number of parallel models will be required to handle frequency selective forecasting.

3) Current works typically assume clean historical data, failing to address the frequent sensor outages and data gaps inherent in real-world EMF monitoring [26].

3) *Generative AI for TSF*: In recent years, generative models have emerged as a powerful paradigm within DL for TSF. Representative architectures include Variational Autoencoders (VAEs) [30], Generative Adversarial Networks (GANs) [31], [32], and, more recently, DMs [7], [33], which have gained remarkable attention for their ability to capture data uncertainty and generate high-fidelity forecasts. DMs, as latent-variable generative frameworks, learn complex data distributions via a dual process of progressive noise injection (the *forward diffusion*) and iterative denoising (the *reverse process*). More recently, DMs have been successfully adapted to time series data [34], [35], offering a flexible generative framework for learning intricate temporal dependencies and stochastic dynamics. While DiffTCN introduces probabilistic modeling, the majority of QoS research remains deterministic.

In the context of TSF, DMs are typically formulated as *conditional generative models*, where the goal is to produce future trajectories conditioned on past observations and optional contextual covariates [30], [34], [36]. During training, Gaussian noise is incrementally added to the ground-truth future sequence through the forward diffusion process, while a neural network, conditioned on historical context, is optimized to learn the inverse mapping that progressively denoises the signal. At inference, forecasts are generated by iteratively sampling and denoising noise vectors, effectively drawing from the learned conditional distribution.

Compared to conventional deterministic or probabilistic models, DMs present several advantages:

- 1) DMs yield fully probabilistic forecasts, enabling uncertainty quantification through multiple stochastic samples and predicting extreme cases in terms of different EMF traffic flows, whereas deterministic models are disadvantaged in capturing uncertainty [37].
- 2) They maintain stable and well-behaved training dynamics, avoiding adversarial divergence;
- 3) They offer a highly modular design that allows flexible conditioning on exogenous factors such as seasonal indicators, control variables, or multimodal inputs [38]–[40].

Empirically, DMs demonstrate competitive or even state-of-the-art results across numerous TSF benchmarks [40]–[44], positioning them as a cornerstone of next-generation generative forecasting frameworks.

III. MULTIVARIATE EMFUSION: CONDITIONAL DM FOR FREQUENCY SELECTIVE EMF FORECASTING

This section details our methodology for multivariate EMF TSF leveraging a conditional DM. Given the sequence of historical EMF measurements and corresponding contextual factors, the goal is to model the conditional distribution of the future EMF values. The proposed model is then enhanced with imputation-based resampling to deal with real-world EMF logs where EMF measurements may be irregularly sampled or there are gaps or sensor outages.

A. Multivariate Conditional Diffusion Model

We consider a multivariate time-series forecasting problem in which each observation $\mathbf{x}_t \in \mathbb{R}^N$ represents measurements from N variates or frequency channels at time t . Given a historical window of length H , denoted by $\mathbf{X}_{\text{past}} = (\mathbf{x}_{T-H+1}, \dots, \mathbf{x}_T)$, the objective is to predict the future multichannel trajectory $\mathbf{X}_{\text{future}} = (\mathbf{x}_{T+1}, \dots, \mathbf{x}_{T+F})$ over a forecast horizon F . To model the conditional distribution $p_\theta(\mathbf{X}_{\text{future}} \mid \mathbf{X}_{\text{past}}, \mathbf{c})$, we introduce an external condition vector \mathbf{c} , which may include calendar features, operational metadata, or other exogenous covariates. Unlike vectorized formulations, we treat the full future window as a matrix $\mathbf{X}_0 := [\mathbf{X}_{\text{past}}, \mathbf{X}_{\text{future}}] \in \mathbb{R}^{(H+F) \times N}$ and apply diffusion directly in this multivariate tensor space. This enables probabilistic forecasting while preserving the temporal–channel structure of the signal.

In the diffusion-based formulation, the forward noising process corrupts the clean \mathbf{X}_0 over T time steps according to the Markov transition process given by [5], [45]:

$$q(\mathbf{X}_t \mid \mathbf{X}_{t-1}) = \mathcal{N}(\sqrt{\alpha_t} \mathbf{X}_{t-1}, (1 - \alpha_t) \mathbf{I}), \quad (1)$$

which admits the closed-form marginal

$$q(\mathbf{X}_t \mid \mathbf{X}_0) = \mathcal{N}(\sqrt{\alpha_t} \mathbf{X}_0, (1 - \bar{\alpha}_t) \mathbf{I}), \quad (2)$$

where $\alpha_t \in (0, 1]$ is a predefined noise schedule, \mathbf{I} denotes the identity matrix, and $\bar{\alpha}_t = \prod_{s=1}^t \alpha_s$, where α_s is the noise intensity of each step in the noise addition process. During training, noisy future samples can be directly sampled from \mathbf{X}_0 at any timestep t , i.e.,

$$\mathbf{X}_t = \sqrt{\alpha_t} \mathbf{X}_0 + \sqrt{1 - \bar{\alpha}_t} \boldsymbol{\epsilon}, \quad \boldsymbol{\epsilon} \sim \mathcal{N}(0, \mathbf{I}), \quad (3)$$

with $\boldsymbol{\epsilon} \in \mathbb{R}^{(H+F) \times N}$ containing i.i.d. Gaussian noise.

The training objective minimizes the discrepancy between the true noise $\boldsymbol{\epsilon}$ and the network-predicted noise $\boldsymbol{\epsilon}_\theta(\mathbf{X}_t, t, \mathbf{c})$ using a mean-squared error loss:

$$L(\theta) = \mathbb{E}_{t, \mathbf{X}_0, \boldsymbol{\epsilon}} \left[\|\boldsymbol{\epsilon} - \boldsymbol{\epsilon}_\theta(\sqrt{\bar{\alpha}_t} \mathbf{X}_0 + \sqrt{1 - \bar{\alpha}_t} \boldsymbol{\epsilon}, t, \mathbf{c})\|^2 \right]. \quad (4)$$

The reverse diffusion process serves as the generative mechanism for forecasting. The conditional reverse diffusion process predicts the distribution $p_\theta(\mathbf{X}_{t-1} \mid \mathbf{X}_t, \mathbf{c})$, of the less

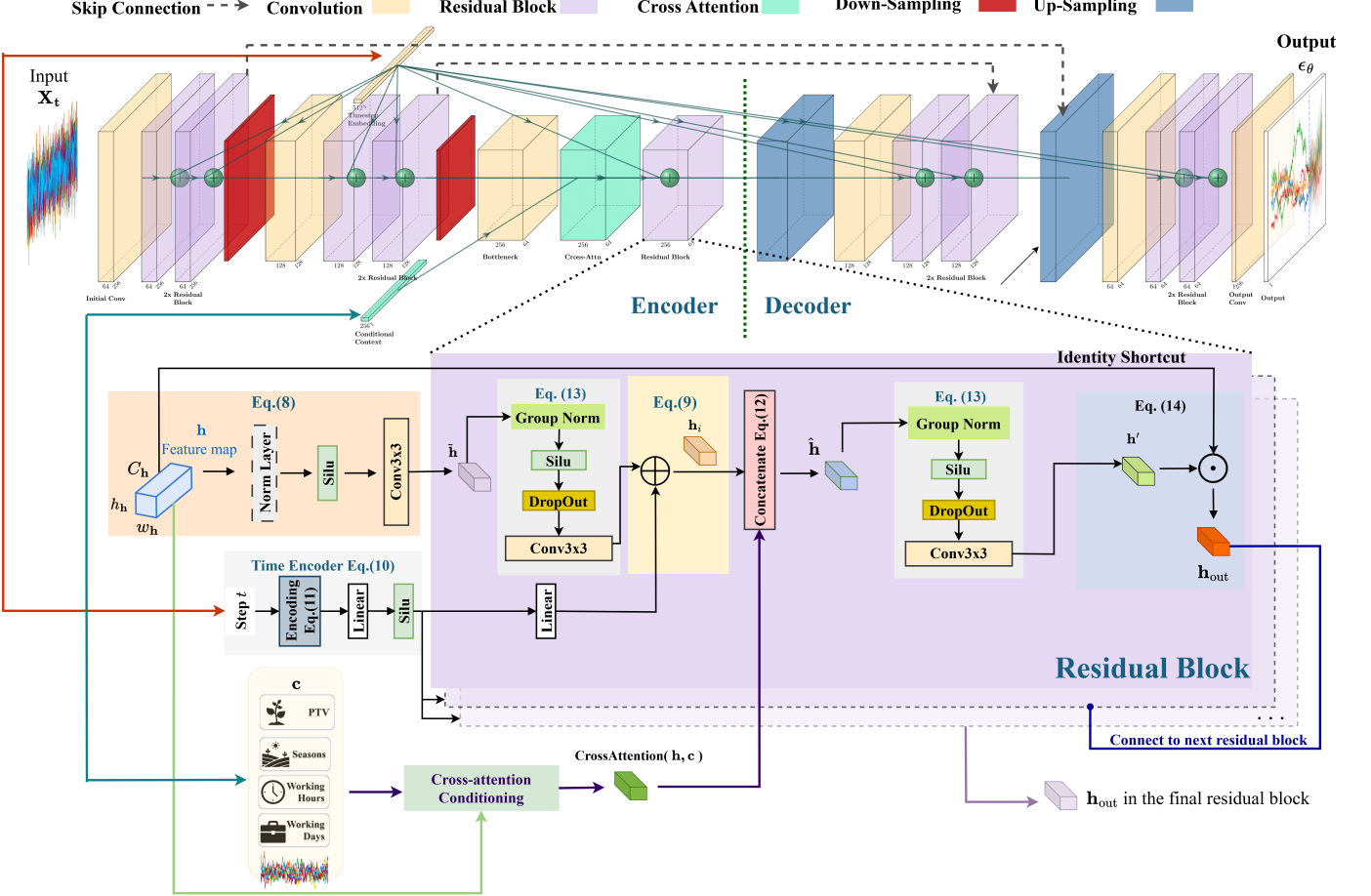


Fig. 1: The U-Net architecture used for EMFusion. The network processes a noisy input through a symmetric encoder-decoder path. Timestep embeddings are incorporated into the residual blocks, while external context is injected via a cross-attention block between the residual blocks of the encoder and decoder. The residual block architecture of EMFusion to estimate $\epsilon_\theta(\cdot)$.

noisy state \mathbf{X}_{t-1} given the current noisy state \mathbf{X}_t and the conditioning information \mathbf{c} . It learns to reconstruct the original signal \mathbf{X}_0 by iteratively denoising the noisy samples, starting from pure noise $\mathbf{X}_T \sim \mathcal{N}(0, \mathbf{I})$. A neural network $\epsilon_\theta(\mathbf{X}_t, t, \mathbf{c})$ is employed to approximate the reverse transition distribution $p_\theta(\mathbf{X}_{t-1} | \mathbf{X}_t, \mathbf{c})$ by predicting the noise component ϵ that was added at step t . This noise prediction network takes the noisy data \mathbf{X}_t , the current timestep t , and the conditioning vector \mathbf{c} to predict the following conditional distribution:

$$p_\theta(\mathbf{X}_{t-1} | \mathbf{X}_t, \mathbf{c}) = \mathcal{N}(\mu_\theta(\mathbf{X}_t, t, \mathbf{c}), \Sigma_\theta(\mathbf{X}_t, t, \mathbf{c})), \quad (5)$$

where the mean computed from ϵ_θ is given by:

$$\mu_\theta(\mathbf{X}_t, t, \mathbf{c}) = \frac{1}{\sqrt{\alpha_t}} \left(\mathbf{X}_t - \frac{1 - \alpha_t}{\sqrt{1 - \bar{\alpha}_t}} \epsilon_\theta(\mathbf{X}_t, t, \mathbf{c}) \right). \quad (6)$$

and \mathbf{c} encapsulates features from the dataset, such as `Italy_WorkingDay`, `Italy_WorkingHour`, and `Italy_Season`, which depict factors influencing EMF variations [43], [44]. By conditioning the noise prediction on \mathbf{c} , the model learns to generate EMF trajectories consistent with temporal continuity and relevant external dependencies.

This formulation enables a fully multivariate, conditionally guided reverse diffusion process in which \mathbf{X}_t is iteratively

denoised using both the historical multichannel window \mathbf{X}_{past} and the external condition vector \mathbf{c} .

During inference, a classifier-free guidance (CFG) mechanism [5], [46] steers the generation process. The final noise prediction is obtained by combining the conditional and unconditional outputs of the denoising network:

$$\hat{\epsilon}_\theta(\mathbf{X}_t, t, \mathbf{c}) = (1 + s_c) \epsilon_\theta(\mathbf{X}_t, t, \mathbf{c}) - s_c \epsilon_\theta(\mathbf{X}_t, t, \emptyset), \quad (7)$$

where s_c is the guidance scale controlling the adherence to the conditioning input \mathbf{c} , and \emptyset represents an unconditional prediction. In conditional TSF, positive CFG scales often over-concentrate the posterior, which narrows prediction intervals. Since our model already injects conditioning via cross-attention, we found $s_c = 0$ is the best via hyperparameter tuning. This conditional diffusion formulation provides the theoretical basis for our model.

B. Model Architecture and Cross-Attention Integration

We employ a U-Net backbone for the noise-prediction network ϵ_θ . As shown in Fig. 1, the U-Net is a deep neural network with multiple residual blocks. The encoder and decoder are symmetric structure, consisting of the same number of residual blocks and additional downsampling or upsampling

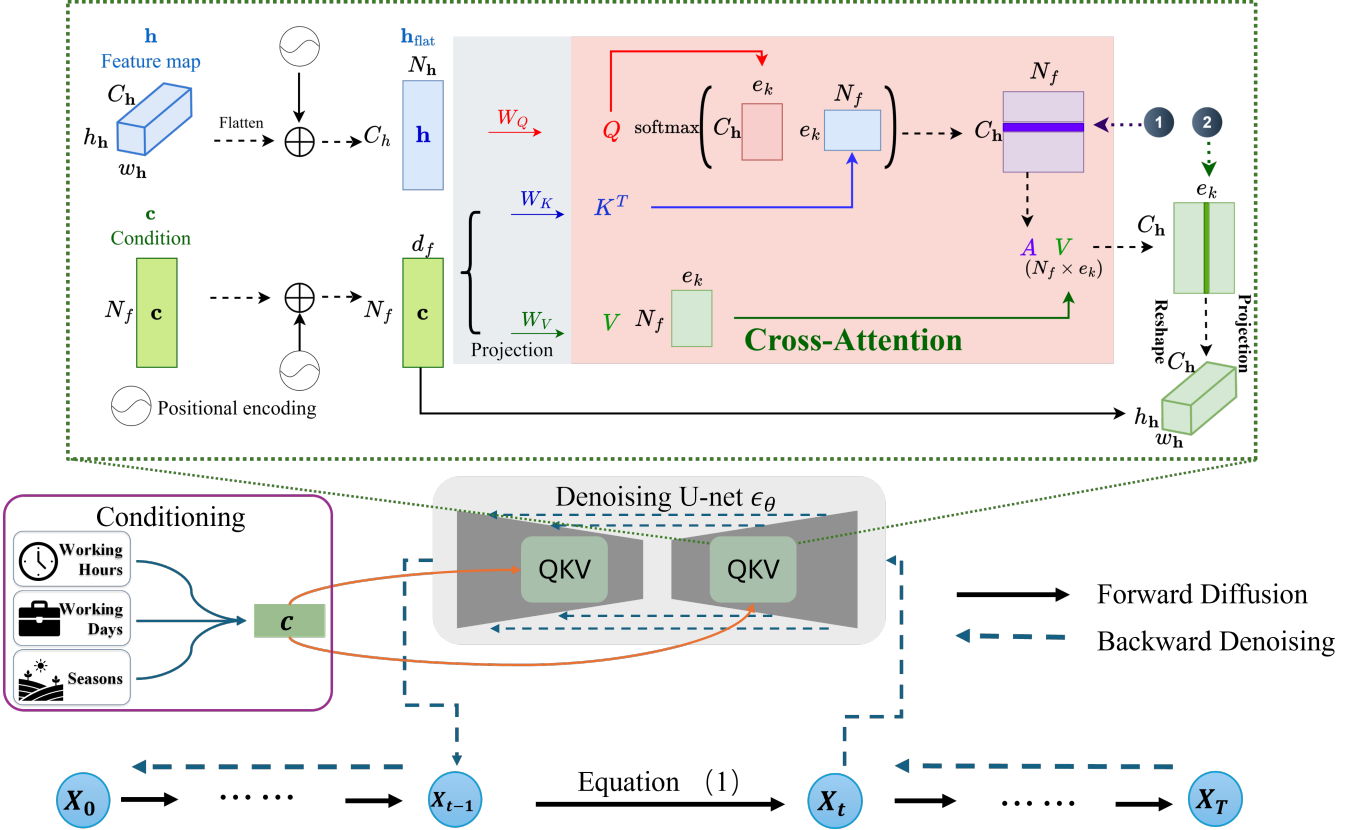


Fig. 2: EMFusion for multivariate frequency selective EMF forecasting with cross-attention.

Algorithm 1: DDPM Training for Multivariate Forecasting with Cross-Attention

Input: $\mathbf{X}_0 = [\mathbf{X}_{\text{past}}, \mathbf{X}_{\text{future}}]$, conditions \mathbf{c}
Output: Learned parameters θ
 Sample $t \sim \mathcal{U}\{1, \dots, T\}$ and noise $\epsilon \sim \mathcal{N}(0, I)$;
 Generate noisy sequence: $\mathbf{X}_t = \sqrt{\bar{\alpha}_t} \mathbf{X}_0 + \sqrt{1 - \bar{\alpha}_t} \epsilon$;
 Pass \mathbf{X}_t and t through U-Net;
 Time series t embedding
for each cross-attention block **do**
 Positional encoding computed by Eq (15);
 Compute $Q = \mathbf{h}_{\text{flat}} W_Q$, $K = \mathbf{c} W_K$, $V = \mathbf{c} W_V$;
 Compute Attention = $\text{Softmax}(QK^\top / \sqrt{e_k})V$;
 Update feature map: $\mathbf{h} \leftarrow \mathbf{h} + \text{Attn}$;
end
 Predict noise with Cross Attention by Eq (12):
 $\hat{\epsilon}_\theta = \epsilon_\theta(\mathbf{X}_t, t, \mathbf{c})$;
 Update parameters by minimizing $\mathcal{L}(\theta) = \|\epsilon - \hat{\epsilon}_\theta\|_2^2$;

block. Each residual block contains convolution to capture local details of the long series, with the input \mathbf{X}_t , condition \mathbf{c} , and time step t . The input multivariate \mathbf{X}_0 passes through the U-Net and is processed by residual block to an intermediate feature map \mathbf{h} (with dimensions $C_h \times h_h \times w_h$), while $\mathbf{h} = \mathbf{X}_t$ in the first layer. Here, C_h is the number of channels in the convolutional layer, h_h and w_h are the spatial height and width of the feature map, respectively.

1) *Residual Block with Time-Step Embedding:* The core of the ϵ_θ network is a stack of residual blocks that progressively

Algorithm 2: DDPM Inference for Multivariate Forecasting with Cross-Attention and Masked Imputation

Input: \mathbf{X}_{past} , mask Ω , conditions \mathbf{c} , unknown future window $\mathbf{X}_{\text{future}}$
Output: Sampled future trajectory $\hat{\mathbf{X}}_{\text{future}}$
 Initialize $\mathbf{X}_T \in \mathbb{R}^{(H+F) \times N} \sim \mathcal{N}(0, I)$,
 $\mathbf{X}_0 = [\mathbf{X}_{\text{past}}, \mathbf{X}_{\text{future}}]$;
for $t = T$ to 1 **do**
 Time series t embedding
 Positional encoding computed by Eq (15);
 Predict noise with Cross Attention by Eq (12);
 $\hat{\epsilon}_\theta = \epsilon_\theta(\mathbf{X}_t, t, \mathbf{c})$;
 Sample $\mathbf{z} \sim \mathcal{N}(0, I)$ if $t > 1$, else $\mathbf{z} = 0$;
 Compute one step denoised estimate:

$$\mathbf{X}'_{t-1} = \frac{1}{\sqrt{\bar{\alpha}_t}} \left(\mathbf{X}_t - \frac{1 - \alpha_t}{\sqrt{1 - \bar{\alpha}_t}} \hat{\epsilon}_\theta \right) + \sigma_t \mathbf{z}$$

 Sample $\epsilon \sim \mathcal{N}(0, I)$ for \mathbf{X}_{past} if $t > 1$, else $\epsilon = 0$;
 Add noise to \mathbf{X}_0 : $\mathbf{X}_{\text{obs}} = \sqrt{\bar{\alpha}_t} \mathbf{X}_0 + \sqrt{1 - \bar{\alpha}_t} \epsilon$;
 Clamp observed values (imputation step):

$$\hat{\mathbf{X}}_{t-1} = \Omega \odot \mathbf{X}_{\text{obs}} + (1 - \Omega) \odot \mathbf{X}'_{t-1}$$
;
end
 Extract $\hat{\mathbf{X}}_{\text{future}}$ from \mathbf{X}_0 ;

refine the feature maps. As shown in Fig. 1, each residual block applies normalization, nonlinearity, convolution, and time step conditioning, followed by a residual shortcut. Given an input feature map \mathbf{h} from the previous layer, the block first applies Group Normalization and a Sigmoid Linear Unit

TABLE II: Frequency f (MHz) allocation for mobile operators and technology band used in the Italian dataset. Each entry shows the antenna factor (α_f) in dB m⁻¹ from Keysight N6850A calibration [47].

Operators	$\mathcal{F}_{\text{Iliad}}$	763.0 (32.8), 1835.0 (31.2), 2150.0 (31.9), 2635.0 (33.2), 3630.0 (36.6)
	\mathcal{F}_{TIM}	773.0 (32.9), 806.0 (33.3), 935.0 (34.7), 2137.0 (31.8), 2137.5 (31.8), 2662.0 (33.3), 2662.5 (33.3), 3760.0 (36.9), 3468.0 (36.0), 3468.5 (36.0), 3469.0 (36.0), 3568.0 (36.3), 3568.5 (36.3)
	\mathcal{F}_{VF}	783.0 (33.0), 816.0 (33.4), 945.0 (34.8), 1870.0 (31.0), 2162.0 (31.9), 2162.5 (31.9), 2647.0 (33.2), 2647.5 (33.2), 3680.0 (36.7)
	\mathcal{F}_{W3}	796.0 (33.2), 955.0 (34.9), 1850.0 (30.9), 2120.0 (31.7), 2585.0 (33.0), 2680.0 (33.4), 3610.0 (36.5)
Technologies	\mathcal{F}_{2G}	935.0 (34.7), 945.0 (34.8), 955.0 (34.9)
	\mathcal{F}_{3G}	2120.0 (31.7), 2137.0 (31.8), 2137.5 (31.8), 2150.0 (31.9), 2162.0 (31.9), 2162.5 (31.9)
	\mathcal{F}_{4G}	763.0 (32.8), 773.0 (32.9), 783.0 (33.0), 796.0 (33.2), 806.0 (33.3), 816.0 (33.4), 1835.0 (31.2), 1850.0 (30.9), 1870.0 (31.0), 2585.0 (33.0), 2635.0 (33.2), 2647.0 (33.2), 2647.5 (33.2), 2662.0 (33.3), 2662.5 (33.3), 2680.0 (33.4)
	\mathcal{F}_{5G}	3468.0 (36.0), 3468.5 (36.0), 3469.0 (36.0), 3568.0 (36.3), 3568.5 (36.3), 3610.0 (36.5), 3630.0 (36.6), 3680.0 (36.7), 3760.0 (36.9)

(SiLU) activation, followed by a 3×3 convolution, i.e., [48]:

$$\tilde{\mathbf{h}} = \text{Conv}_1(\sigma(\text{GN}(\mathbf{h}))), \quad (8)$$

where $\text{GN}(\cdot)$ denotes GroupNorm, $\sigma(\cdot)$ is the SiLU activation, and Conv_1 is a 3×3 convolution.

A critical component of the block is the injection of the diffusion step embedding. The global timestep embedding \mathbf{t}^e is passed through a block-specific linear layer and then added to the intermediate feature map:

$$\mathbf{h}_i = \tilde{\mathbf{h}} + \text{Linear}_t(\sigma(\mathbf{t}^e)), \quad (9)$$

where Linear_t maps $\mathbf{t}^e \in \mathbb{R}^{d_{\text{emb}}}$ to the channel dimension of the block, and the result is broadcast across spatial dimensions. This makes the block's behavior explicitly adaptive to the current diffusion step t .

To incorporate the diffusion timestep to the residual block and enrich its effective information, a sinusoidal time embedding is employed to expand its dimension. The timestep t is first mapped into a positional embedding vector \mathbf{t}^e as

$$\mathbf{t}^e = \text{Concat} \left(\begin{bmatrix} \cos(t \cdot \omega_0), \dots, \cos(t \cdot \omega_{\frac{d}{2}-1}) \\ \sin(t \cdot \omega_0), \dots, \sin(t \cdot \omega_{\frac{d}{2}-1}) \end{bmatrix} \right), \quad (10)$$

For a given dimension index m where $0 \leq m < C_h/2$, the frequencies are defined as follows:

$$\omega_m = \exp(-\ln(10000) \cdot \frac{2m}{C_h}) \quad (11)$$

We integrate condition \mathbf{c} into the feature map using cross-attention operation as shown below (more details of the cross-attention are given in the following subsection and Fig. 2):

$$\hat{\mathbf{h}} = \mathbf{h}_i + \text{CrossAttention}(\mathbf{h}, \mathbf{c}). \quad (12)$$

The updated feature map $\hat{\mathbf{h}}$ is then processed by a second sequence of operations, GroupNorm, SiLU, dropout, and another

3×3 convolution [48]:

$$\mathbf{h}' = \text{Conv}_2(\text{Dropout}(\sigma(\text{GN}(\hat{\mathbf{h}}))). \quad (13)$$

Finally, a residual shortcut is applied as [49]:

$$\mathbf{h}_{\text{out}} = \mathbf{h}' + \text{Shortcut}(\mathbf{h}), \quad (14)$$

where Shortcut is the identity mapping for feature mining and convolution operation for up sampling and down sampling. By stacking these modules in the encoder, the series is processed shorter and the convolution channels increase, so that abstract temporal and spatial information are extracted.

2) *Cross-Attention Module*: To integrate conditioning information, instead of simple concatenation, we use cross-attention modules at multiple layers in both the encoder and decoder, as depicted in Fig. 2. This allows the model to dynamically attend to the most relevant parts of the conditioning information at different stages of processing and across different temporal scales. The condition tensor \mathbf{c} (with dimensions $N_f \times d_f$) and the intermediate feature map \mathbf{h} are two inputs of the cross-attention module. Note that N_f is the sequence length of the condition and d_f is its feature dimension.

To compute the attention, the 3D feature map \mathbf{h} is first flattened into a 2D tensor, \mathbf{h}_{flat} , with shape (C_h, N_h) , where $N_h = h_h \cdot w_h$. Since cross-attention calculation basically contains linear connection without recurrence, it's important to fully make use of the order of the sequence. Positional encoding adds positional information to \mathbf{c} and \mathbf{h}_{flat} , which helps the module extract temporal and spatial correlations. Consequently, we add positional encoding to \mathbf{c} and \mathbf{h}_{flat} according to [50]:

$$\mathbf{c} \leftarrow \mathbf{c} + \text{PE}(\mathbf{c}) \in \mathbb{R}^{N_f \times d_f} \quad (15)$$

$$\mathbf{h}_{\text{flat}} \leftarrow \mathbf{h}_{\text{flat}} + \text{PE}(\mathbf{h}_{\text{flat}}) \in \mathbb{R}^{C_h \times N_h} \quad (16)$$

$$\text{PE}(\cdot) = \begin{cases} \text{PE}_{(p,2i)} = \sin(p/10000^{2i/d_{\text{series}}}), \\ \text{PE}_{(p,2i+1)} = \cos(p/10000^{2i/d_{\text{series}}}), \end{cases} \quad (17)$$

where p and i denote the position and the dimension index of the input series, respectively, and d_{series} is the embedding dimension of the sequence.

The cross-attention module operates between the feature map and the conditional embeddings, allowing the model to explicitly learn their correlations and dynamically modulate its representations based on the provided conditions. Its calculation is based on QKV where the Queries (Q) are projected from this flattened feature map, while the Keys (K) and Values (V) are projected from the conditioning tensor \mathbf{c} , i.e.,

$$Q = \mathbf{h}_{\text{flat}} W_Q, \quad K = \mathbf{c} W_K, \quad V = \mathbf{c} W_V \quad (18)$$

where W_Q , W_K , and W_V are learnable weight matrices [5], [51]. The attention matrix A and the final output are calculated using the standard scaled dot-product attention mechanism:

$$\text{CrossAttention}(\mathbf{h}, \mathbf{c}) = \text{Softmax}\left(\frac{QK^T}{\sqrt{e_k}}\right)V = AV, \quad (19)$$

where e_k is the dimension of the keys (and queries), used for scaling. According to ① in Fig. 2, a single row of the attention matrix A represents the set of attention weights that one specific element from the flattened feature map \mathbf{h}_{flat} (represented by a row of Q) pays to all N_f elements of the condition vector \mathbf{c} (represented by the rows of K). ② in Fig. 2 shows a column of the value V that corresponds to a feature map weighted by the attention in A [52]. The output of this operation, AV , represents the contextually relevant information from \mathbf{c} , weighted according to its relevance to \mathbf{h} . This output is then reshaped and projected to match the original feature map's dimensions ($C_h \times h_h \times w_h$). This result is finally added back to the original feature map \mathbf{h} via a residual connection, which is shown in the previous section:

$$\mathbf{h}' = \mathbf{h} + \text{CrossAttention}(\mathbf{h}, \mathbf{c}).$$

In this context, $\text{CrossAttention}(\cdot)$ in Eq. (12) represents the full module's operation, including the final reshape and projection steps shown in the diagram. According to ② in Fig. 2, a single column of the final output (AV) is the new vector representation for that specific feature map element. It is calculated as the weighted sum of all N_f rows of the Value matrix V . The weights used for this sum are the attention scores from the corresponding row of A .

C. EMFusion Training and Inference

The cross-attention integrated U-Net learns to predict noise in the training phase as Algorithm 1. Given the full window $\mathbf{X}_0 = [\mathbf{X}_{\text{past}}, \mathbf{X}_{\text{future}}]$ and the conditions \mathbf{c} , the first step is to randomly choose a $t \sim \mathcal{U}\{1, \dots, T\}$ and noise $\epsilon \sim \mathcal{N}(0, I)$ to add noise to the original sequence \mathbf{X}_0 by using Eq. (3): $\mathbf{X}_t = \sqrt{\alpha_t} \mathbf{X}_0 + \sqrt{1 - \alpha_t} \epsilon$. The task of the U-Net is to learn the ability to predict ϵ given $\mathbf{X}_t, t, \mathbf{c}$. Pass \mathbf{X}_t through U-Net and generate intermediate feature map \mathbf{h} . Then embed positional information to \mathbf{c} and \mathbf{X}_0 and calculate cross-attention between \mathbf{h} and \mathbf{c} when going through cross-attention blocks. Subsequently the output noise $\hat{\epsilon}_\theta$ is the same dimension as ϵ . By minimizing MSE loss $\mathcal{L}(\theta) = \|\epsilon - \hat{\epsilon}_\theta\|_2^2$, the model updates itself and learn to predict noise based on any t . Then

the well-trained model participates in the denoising process in the inference phase by predicting noise $\hat{\epsilon}_\theta = \epsilon_\theta(\mathbf{X}_t, t, \mathbf{c})$ at each step t and the conditions are input through cross-attention module, as shown in Algorithm 2.

D. Imputation-Based Sampling at the Inference

In practical EMF monitoring, historical measurements are often uneven, partially observed, or corrupted due to sensor outages, data-handling issues, and privacy-related filtering, resulting in time series with substantial gaps and irregular sampling. Such incomplete inputs limit the effectiveness of pure conditional forecasting, which assumes fully reliable past observations. An imputation-based diffusion formulation addresses this limitation by treating both missing past values and all future values as unobserved entries of a single masked sequence. During the DDPM reverse process, the model performs principled generative inpainting—reconstructing irregular or missing segments of the past while simultaneously generating future values under the same probabilistic dynamics. Since past and future EMF measurements lie on the same underlying temporal manifold, casting forecasting as structured inpainting enables the model to learn cross-temporal dependencies across the entire sequence.

To handle both forecasting and imputation within a unified framework, we adopt a masked conditional DDPM that models the full sequence $\mathbf{X}_0 = [\mathbf{X}_{\text{past}}, \mathbf{X}_{\text{future}}]$ under partial observations. That is, the model receives a concatenated input sequence \mathbf{X}_0 consisting of a known historical window \mathbf{X}_{past} and an unknown future window $\mathbf{X}_{\text{future}}$ that is initially masked. The objective is to infer the missing future segment in a manner that is probabilistically consistent with \mathbf{X}_{past} . The algorithmic realization is summarized in Algorithm 2.

Let Ω denotes a binary observation mask (for the i -th element, $\Omega_i = 1$ for observed entries and $\Omega_i = 0$ for missing ones), and let $\mathbf{X}_{\text{obs}} = \sqrt{\alpha_t} \mathbf{X}_0 + \sqrt{1 - \alpha_t} \epsilon$, $\epsilon \sim \mathcal{N}(0, I)$, denotes the available measurements. As in standard diffusion models, the forward process gradually perturbs the clean sequence \mathbf{X}_0 with Gaussian noise as in (3), while the model learns a masked conditional reverse process, i.e., (5) still applies by adding conditions on \mathbf{c} . The noisy sequence is processed through the conditional U-Net $\epsilon_\theta(\mathbf{X}_t, t, \mathbf{c})$ to obtain a one-step denoised estimate of the entire trajectory, denoted as $\hat{\mathbf{X}}_{t-1}$. After each denoising step, the observed entries are clamped to their known values to ensure consistency:

$$\hat{\mathbf{X}}_{t-1} = \Omega \odot \mathbf{X}_{\text{obs}} + (1 - \Omega) \odot \mathbf{X}'_{t-1}, \quad (20)$$

where $\hat{\mathbf{X}}_{t-1}$ denotes the model's predicted denoised sample at timestep $t-1$.

$$\hat{\mathbf{X}}_{t-1} = \frac{1}{\sqrt{\alpha_t}} \left(\mathbf{X}_t - \frac{1 - \alpha_t}{\sqrt{1 - \alpha_t}} \hat{\epsilon}_\theta \right) + \sigma_t \mathbf{z} \quad (21)$$

After T iterations of the denoising process, a predicted sequence $\hat{\mathbf{X}}_{\text{future}}$ can be obtained from $\hat{\mathbf{X}}_0$. This mechanism enables the DM to impute with past values and generate future trajectories within the same sampling procedure. The training objective follows the standard noise-prediction loss as in (4) with masked conditioning. If we sample \hat{N} times, a set of

\hat{N} predicted sequences $\mathbf{S} = \{\hat{\mathbf{X}}_{\text{future}}^i\}_{i=1,\dots,\hat{N}}$ is ready for probabilistic interval construction which is explained next.

E. Probabilistic Interval Construction

Subsection III-E describes probabilistic interval construction for calibrated uncertainty quantification. The procedure begins once the EMFusion has generated an ensemble of \hat{N} distinct future EMF trajectories $\mathbf{S} = \{\hat{\mathbf{X}}_{\text{future}}^i\}_{i=1,\dots,\hat{N}} \in \mathbb{R}^{\hat{N} \times F}$ for each of the N monitored carriers (e.g., individual 2G, 3G, 4G, and 5G carriers across multiple operators). For each future time step $k \in \{1, 2, \dots, F\}$, this yields a set of \hat{N} predicted values, denoted as $\mathbf{Z} = \{z_1, z_2, \dots, z_{\hat{N}}\}$. This ensemble can be viewed as a discrete, non-parametric sample drawn from the learned conditional predictive distribution. To convert this sample set into a continuous probability density function (PDF), Kernel Density Estimation (KDE) is employed [5]. KDE is a classical non-parametric technique that estimates the underlying density $f(z)$ by placing a kernel function, typically Gaussian, at each sample point and summing the contributions:

$$f(z) = \frac{1}{\hat{N} \cdot s_p} \sum_{i=1}^{\hat{N}} K\left(\frac{z - z_i}{s_p}\right), \quad (22)$$

where $K(\cdot)$ is the kernel function and s_p is the bandwidth parameter. The bandwidth s_p is crucial for controlling smoothness, determining the bias and variance trade-off in the estimated density. This nonparametric statistical method can directly estimate probability distributions from discrete scenarios without requiring prior assumptions about the distribution. Once the PDF $f(z)$ is derived, the cumulative distribution function $F(z)$ is computed, and the prediction interval is obtained via quantile extraction. Specifically, for a target confidence level γ , the lower and upper quantile bounds $q_{\underline{\alpha}}$ and $q_{\bar{\alpha}}$ satisfy $PI_{\gamma} = [q_{\underline{\alpha}}, q_{\bar{\alpha}}]$, $q_{\alpha} = F^{-1}(\alpha)$, where $\gamma = \bar{\alpha} - \underline{\alpha}$, and $\underline{\alpha}$, $\bar{\alpha}$ denote the lower and upper quantile levels, respectively.

In most KDE-based interval estimation scenarios, symmetric intervals satisfying $\bar{\alpha} + \underline{\alpha} = 1$ are adopted. In this work, however, since EMFusion directly generate multiple stochastic trajectories, we employ a simplified empirical interval construction approach. Specifically, given sorted samples $z_1 < z_2 < \dots < z_{\hat{N}}$, the interval PI_{γ} is directly determined from the corresponding order statistics without KDE, offering a computationally efficient alternative:

$$\hat{N}_{\gamma} = \lfloor (1 - \gamma) \cdot \hat{N} \rfloor \quad (23)$$

$$PI_{\gamma} = [z_{\hat{N}_{\gamma}}, z_{\hat{N} - \hat{N}_{\gamma}}] \quad (24)$$

F. Univariate Forecasting: A Special Case

As illustrated in Fig. 3, Univariate forecasting illustrates the aggregate-then-learn paradigm, where multiple time series are first aggregated before applying the forecasting model. Multivariate forecasting the learn-then-aggregate paradigm, where forecasts are generated for each frequency series individually and then aggregated. In the EMFusion framework, the main differences between the univariate and multivariate

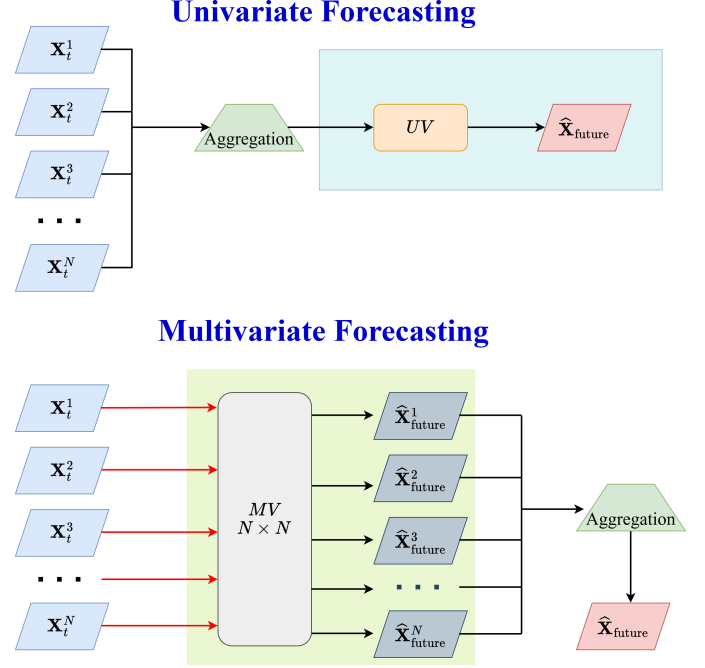


Fig. 3: Comparison of univariate (UV) and multivariate (MV) forecasting strategies for EMF time-series across N features.

instantiations of EMFusion are confined to the input dimensionality and the associated architectural hyperparameters. In the multivariate setting ($N > 1$), the input \mathbf{X}_0 is treated as a 2-D tensor, processed via 2-D convolutional layers to simultaneously capture temporal evolution and inter-frequency correlations. Conversely, the univariate configuration ($N = 1$) utilizes 1-D convolutions, focusing exclusively on temporal dynamics. In the univariate setting, the model receives a single narrow-band EMF time series and the input tensor is of shape $(B, H, 1)$, where B is the batch size and H is the look-back length, thus we employ 1-D convolutions. In the multivariate setting, the input at each time step lead to an input tensor of shape (B, H, N) and 2-D convolutions acting jointly on time and frequency. When computing cross-attention, the univariate uses a single hidden channel $h_h = 1$ in the value projection (effectively attending only along time), whereas the multivariate sets $h_h > 1$ so that attention can propagate information both temporally and across bands.

IV. DATA SPECIFICATIONS AND ANALYSIS

This section details dataset specifications including the measurement set-up, received power (dBm) to electric-field (Volts per meter) conversion, and the external conditioning factors. The top two plots in Fig. 4 show the time evolution¹ of operator-specific EMF levels in the Italian dataset. The operator-wise difference in EMF levels is notable. Iliad systematically dominates the total exposure, with a typical peak at 0.8 V/m. W3 provides the second-largest contribution on EMF, while TIM and VF remain consistently lower, with most values below 0.3 V/m. This suggests antenna being placed

¹The data were collected at the University Hospital Tor Vergata in Rome, Italy, from 2023-07-26 16:49:02 to 2024-03-11 05:08:28.

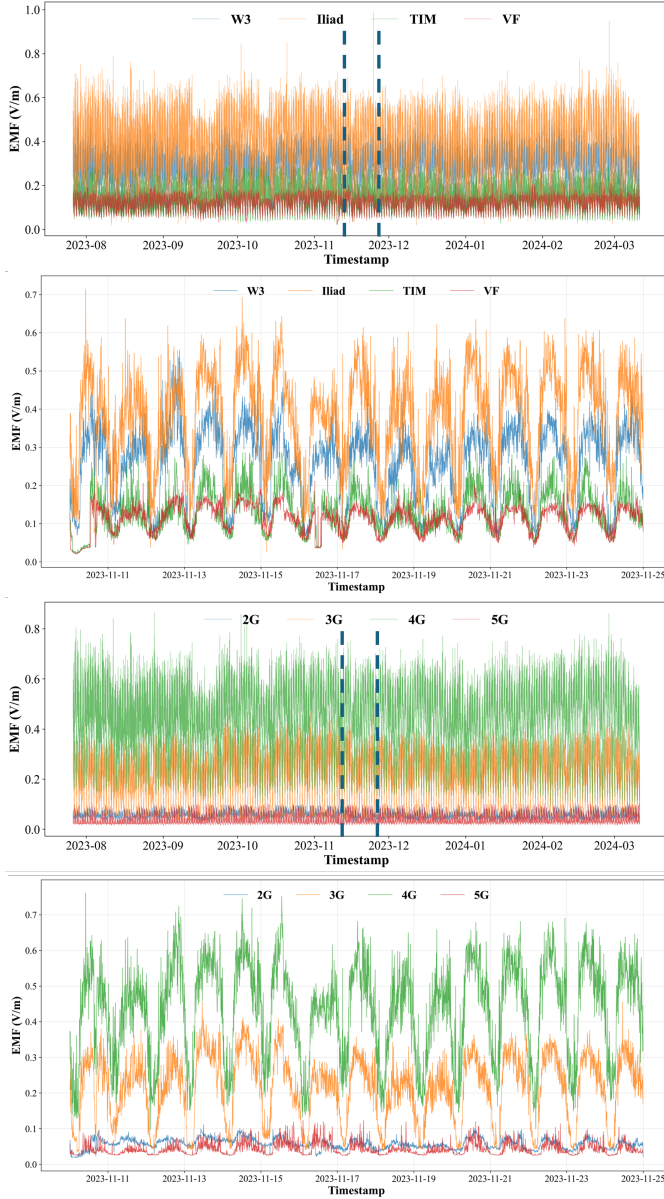


Fig. 4: EMF levels in Italian dataset, as a function of network operators (1,2) and cellular technologies (3,4). The plots (1,3) display the 8-month trend (Aug 2023 – Mar 2024), while the plots (2,4) show enlarged 14-day daily trend.

in the University hospital or a configuration that produced a stronger signal at the specific point of measurement in favour of Iliad. Moreover, while the other operators display broadly similar deployment and load patterns, Iliad follows a more independent deployment and load profile, with a narrower spectrum allocation in the mid-band 5G frequencies compared to the other operators.

On the other hand, the bottom two plots in Fig. 4 depict that the EMF level from 4G clearly dominates the total EMF levels from 2G, 3G, or 5G technologies, both in terms of average level and short-term variability, with typical peaks reaching 0.8 V/m. The 3G contribution is noticeably smaller but still non-negligible, while 2G and 5G produce the lowest fields, generally below 0.1 V/m except for a few isolated peaks.

This trend is likely due to the sparse deployment of both 2G and 5G technologies and widespread deployment of 4G at the time of measurements. Both operator-wise and technology-wise display the recurrent daily cycle and stable behaviour over the months. According to Fig. 5, 4G is only weakly correlated with the other technologies ($\rho \leq 0.19$), whereas 5G exhibits a moderate correlation with 2G and 3G. This behavior is consistent with the technological innovations introduced in 4G and 5G with respect to legacy generations, such as active antennas, beamforming, MIMO, and time-division duplexing.

A. Dataset Specifications

The received power measurements were collected continuously from July 26, 2023 to March 10, 2024 across 29 frequency channels spanning from 9 kHz - 6GHz. The dataset is then organized according to the predefined frequency bands of major Italian network operators and the corresponding cellular technologies. Table II summarizes the frequency allocations used by each operator and technology.

1) *EMF Monitoring Set-up*: The EMF monitoring chain couples an omnidirectional antenna, an Anritsu MS27102A remote spectrum-monitoring unit, and the ARPA-Lazio *Search24* control software [53]. The Keysight N6850A passive antenna [47] is connected to the portable spectrum analyzer via a 1.5 m low-loss coaxial cable. The antenna delivers uniform gain across all licensed cellular bands up to the 3.6 GHz. The weather-proof MS27102A sweeps 9 kHz–6 GHz continuously and, thanks to its internal pre-selector, outputs real-time narrow-band channel power while operating unattended on a rooftop site [54]. *Search24* [55] scripts enable streaming the data to a local computer over a dedicated Ethernet link.

2) *Conversion of Received Power to EMF*: The received power for a given frequency channel f at the output of the antenna is measured in dBm. For a given frequency f , the received power is then converted into the electric-field strength (measured in V/m) as given below [2]:

$$E_f = \sqrt{\frac{P_r(f) Z_0}{A_e(f)}} = \sqrt{\frac{10^{\frac{P_{\text{dBm}}(f)-30}{10}} Z_0}{A_e(f)}} \quad (25)$$

where $Z_0 \approx 376.73 \Omega$, which is the intrinsic (wave) impedance of free space. For a measurement antenna with linear gain G_f , the effective aperture $A_e(f)$ is defined as follows:

$$A_e(f) = \frac{G_f \lambda_f^2}{4\pi}, \quad \lambda_f = \frac{c}{f}, \quad G_f = \left(\frac{A_{GC}}{\lambda_f \cdot 10^{\alpha_f/20}} \right)^2 \quad (26)$$

where c is the speed of light. A_{GC} is antenna-gain calibration constant. The antenna factor α_f changes as a function of frequency f as in [53], [56].

3) *External Conditions*: User activity patterns, driven by work schedules and lifestyle habits, directly influence device usage and consequently the received power and EMF levels. To account for these temporal variations, calendar-based contextual information is incorporated as an external conditioning signal for EMF prediction. For each observation with time stamp t , three features were appended:

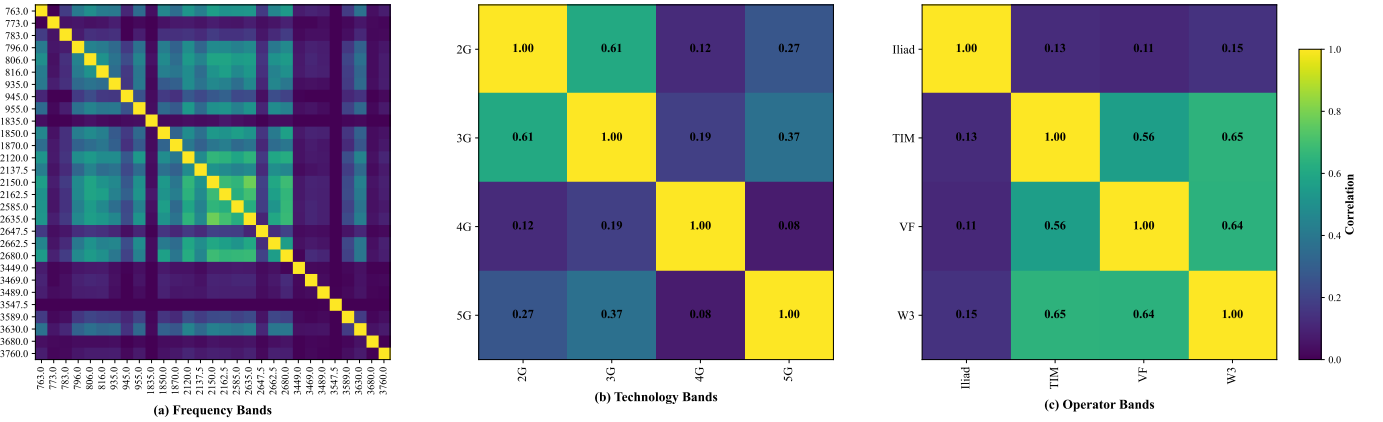


Fig. 5: Correlation maps of EMF levels for (a) frequency bands, (b) cellular technologies, and (c) network operators.

- **Italy_WorkingDay** $\in \{0, 1\}$: indicates whether t falls on a weekday (Monday–Friday) and is not listed in the Italian public-holiday calendar.²
- **Italy_WorkingHour** $\in \{0, 1\}$: equals 1 when the local clock time lies inside the standard business window [09:00, 17:00) and 0 otherwise.
- **Italy_Season** $\in \{1, 2, 3, 4\}$: a flag assigned based on the astronomical equinox–solstice boundaries, i.e., 1) *Spring*: March 21 to June 20; 2) *Summer*: June 21 to September 22; 3) *Autumn*: September 23 to December 20; and 4) *Winter*: December 21 to March 20 in the next year.
- **Italy_Multi** $\in \{1, 2, 3, 4\} \times \{0, 1\}$: a two-dimensional multi-condition feature obtained by concatenating *Italy_Season* and *Italy_WorkingDay*.

B. EMF Classification and Correlation Analysis

From Table II, the aggregate EMF associated with any given operator or cellular technology can be obtained as follows:

$$E_{\mathcal{F}_\chi}(t) = \left(\sum_{f \in \mathcal{F}_\chi} E_f^2 \right)^{1/2}, \quad (27)$$

where $\mathcal{F}_\chi \in \{2G, 3G, 4G, 5G, TIM, VF, W3, Iliad\}$. As an illustration, the 2G band corresponds to the frequency set $\mathcal{F}_{2G} = \{935.0, 945.0, 955.0\}$ MHz, so the aggregate 2G EMF can be computed as $E_{2G}(t) = \sqrt{E_{935.0}^2 + E_{945.0}^2 + E_{955.0}^2}$.

Fig. 5(a) depicts the correlation of EMF among all frequencies. We note that the EMF levels across the bands (e.g., 700–900 MHz, 1800–2100 MHz, 2.6 GHz, and 3.4–3.8 GHz) tend to be more strongly correlated with each other indicating that exposure dynamics are largely driven by co-located carriers within the same spectral neighbourhood.

Fig. 5(b) depicts the correlation of EMF observed among the cellular technologies in the Italian dataset. 2G and 3G exhibit the strongest off-diagonal correlation ($\rho \approx 0.61$), reflecting similar temporal usage patterns of legacy technologies at this

²The holiday list covers national and widely observed regional holidays for 2023–2024, including Easter, Liberation Day, Labour Day, Republic Day, Ferragosto, All Saints' Day, Immaculate Conception, and the Christmas–New Year period. It also includes the university closure date and no teaching activities dates for Università degli Studi di Roma Tor Vergata. [57]

location. In contrast, 4G is only weakly correlated with the other technologies ($\rho \leq 0.19$), while 5G shows moderate correlation with 2G and 3G ($\rho \approx 0.27$ –0.37).

The EMF correlation map (Fig. 5(c)) reveals a high correlation among TIM, VF, and W3, with pairwise correlations in the range $\rho \approx 0.56$ –0.65, while Iliad remains only weakly correlated with the other operators ($\rho \approx 0.11$ –0.15). This indicates that the EMF exposure patterns of the three incumbent operators are highly synchronized at the hospital site, whereas Iliad follows a more independent deployment and load profile.

V. NUMERICAL RESULTS AND DISCUSSIONS

This section presents a comprehensive evaluation of the proposed EMFusion model against state-of-the-art benchmarks. To assess forecasting performance, we define both deterministic (point) and probabilistic forecasts metrics followed by the key baselines and evaluation settings.

A. Evaluation Metrics

Let y_i denote the true observed value at time step i , \hat{y}_i the corresponding median (p50) point forecast produced by the model, and m the total number of samples in the test set. In what follows, we describe the point forecast and

1) *Point Forecast Metrics*: evaluate the accuracy of a single predicted value (the median) against the true value. The considered metrics are listed as follows:

• **Mean Absolute Percentage Error (MAPE)**: measures the average percentage difference between the predicted and actual values, and is defined as follows:

$$\text{MAPE} = \frac{100}{m} \sum_{i=1}^m \frac{|y_i - \hat{y}_i|}{|y_i|} \quad (28)$$

• **Normalized Deviation (ND)**: ND metric measures the total absolute error relative to the total magnitude of the true values, is defined as follows:

$$\text{ND} = \frac{\sum_{i=1}^m |y_i - \hat{y}_i|}{\sum_{i=1}^m |y_i|} \quad (29)$$

• **Root Mean Square Error (RMSE) and Normalized RMSE (NRMSE)**: RMSE measures the standard deviation

TABLE III: A comparative analysis of univariate forecasting performance of EMFusion with imputation without external conditions. Metrics are ordered as CRPS, ND, NRMSE, MAPE, and PICP. Lower is better for CRPS, ND, NRMSE, MAPE; higher is better for PICP. **Bold** = best in column; underline = second best in column.

		Operator-wise Performance																			
Model		Iliad				TIM				VF				W3							
		CRPS	ND	NRMSE	MAPE	PICP	CRPS	ND	NRMSE	MAPE	PICP	CRPS	ND	NRMSE	MAPE	PICP	CRPS	ND	NRMSE	MAPE	PICP
NF		0.0224	0.1901	0.2271	22.0056	69.36	0.0110	0.2674	0.3344	30.5366	<u>65.99</u>	0.0057	0.1505	0.1899	16.3322	<u>69.26</u>	0.0134	0.1732	0.2126	19.5926	72.44
IQLSTM		0.0208	0.1742	0.2088	22.0082	<u>69.61</u>	0.0098	0.2272	0.2905	23.7362	65.43	0.0060	0.1484	0.2158	16.5989	64.66	0.0146	0.1742	0.2179	19.3497	<u>67.87</u>
DDPM		0.0281	0.2266	0.2752	24.7179	75.38	0.0131	0.3078	0.4063	35.0737	76.78	0.0067	0.1741	0.2173	19.2858	90.22	0.0338	0.3945	0.4217	42.9547	28.02
VAE		0.0255	0.2040	0.2424	24.0345	54.86	0.0121	0.2880	0.3504	33.7195	53.63	0.0063	0.1630	0.2040	17.8781	58.19	0.0146	0.1842	0.2236	21.5268	66.11
LSTM-Dropout		0.0311	0.2298	0.2626	32.2884	33.07	0.0137	0.2944	0.3334	38.0923	31.38	0.0072	0.1687	0.2004	20.5388	31.19	0.0232	0.2515	0.2747	34.6254	31.17
WGAN		0.0237	0.1856	0.2216	21.6153	50.18	0.0207	0.3413	0.3809	44.7403	0.00	<u>0.0055</u>	<u>0.1419</u>	0.1780	15.6357	60.28	0.0138	0.1741	0.2096	20.5489	62.22
TimeGrad (29)		0.0329	0.3405	0.8942	89.2536	—	<u>0.0094</u>	0.4230	1.3310	52.4586	—	0.0084	0.2997	1.0983	29.7099	—	0.0203	0.3184	1.0497	48.2214	—
TimeGrad (8)v2		0.0552	0.1790	0.5465	26.7691	—	0.0271	0.3545	1.1546	34.5811	—	0.0201	0.1785	1.0200	<u>15.6345</u>	—	0.0367	0.2124	0.7484	18.9919	—
EMForecaster		0.0243	<u>0.1706</u>	0.2019	21.5334	34.50	0.0103	<u>0.2042</u>	0.2499	22.5550	29.67	0.0061	<u>0.1419</u>	0.2031	16.0613	44.94	0.0147	<u>0.1585</u>	0.1937	<u>18.5124</u>	37.61
EMFusion		0.0169	0.1304	0.1772	14.2795	50.40	0.0067	0.1433	0.2143	14.1847	58.51	0.0043	0.0997	<u>0.1781</u>	11.0273	52.25	0.0099	0.1132	0.1639	12.1131	52.19

		Technology-band-wise Performance																			
Model		2G				3G				4G				5G							
		CRPS	ND	NRMSE	MAPE	PICP	CRPS	ND	NRMSE	MAPE	PICP	CRPS	ND	NRMSE	MAPE	PICP	CRPS	ND	NRMSE	MAPE	PICP
NF		0.0028	0.1416	0.1773	14.3473	59.79	0.0150	0.2153	0.2534	24.2409	62.59	0.0217	0.1637	0.1983	18.1657	<u>69.23</u>	0.0024	0.2103	0.3111	18.5137	72.20
IQLSTM		<u>0.0027</u>	0.1342	0.1708	<u>13.7036</u>	56.70	<u>0.0134</u>	0.1841	0.2256	20.9445	<u>63.17</u>	0.0210	<u>0.1488</u>	<u>0.1827</u>	<u>17.1465</u>	66.22	0.0028	0.1901	<u>0.2994</u>	<u>18.1656</u>	66.50
DDPM		0.0029	0.1462	0.1858	15.0905	82.02	0.0150	0.2132	0.2536	26.5512	76.83	0.0267	0.1890	0.2345	19.6537	74.21	0.0031	0.2536	0.3570	24.2072	<u>71.12</u>
VAE		0.0028	0.1429	0.1786	14.3644	<u>60.92</u>	0.0168	0.2227	0.2606	26.1413	45.59	0.0237	0.1698	0.2051	19.2985	58.84	0.0028	0.2298	0.3246	21.2987	57.09
LSTM-Dropout		0.0033	0.1388	<u>0.1699</u>	14.4200	32.48	0.0196	0.2728	0.2991	44.0706	48.00	0.0294	0.1994	0.2273	24.2642	39.79	0.0038	0.2742	0.3224	28.7500	14.29
WGAN		0.0028	0.1374	0.1747	13.7520	53.91	0.0146	0.2003	0.2339	23.7100	54.25	0.0224	0.1556	0.1903	17.8671	51.53	0.0046	0.2674	0.3303	26.9596	0.00
TimeGrad (29)		0.0059	0.3761	2.2558	38.7363	—	0.0267	0.3133	0.9559	61.6179	—	0.0190	0.3375	0.9451	56.1075	—	0.0051	0.3912	0.9879	40.6475	—
TimeGrad (8)v2		0.0072	0.1746	1.9840	16.9011	—	0.0339	0.2040	0.6425	24.7493	—	0.0584	0.1888	0.6344	21.9084	—	0.0111	0.3741	1.0243	21.8487	—
EMForecaster		0.0104	0.1682	0.2156	19.0429	37.40	0.0139	<u>0.1688</u>	0.2122	19.6655	36.68	0.0134	0.1661	0.2102	19.3257	37.34	0.0128	<u>0.1802</u>	0.2262	20.6762	34.69
EMFusion		0.0016	0.0821	0.1135	8.3460	59.64	0.0085	0.1153	0.1564	13.1791	52.88	<u>0.0169</u>	<u>0.1109</u>	0.1495	11.8418	55.69	0.0019	0.1518	0.4311	11.5743	66.95

of the prediction errors. NRMSE normalizes RMSE by the root mean square of the true values, facilitating comparison across datasets with different scales.

$$\text{RMSE} = \sqrt{\frac{1}{m} \sum_{i=1}^m (y_i - \hat{y}_i)^2} \quad (30)$$

$$\text{NRMSE} = \frac{\text{RMSE}}{\sqrt{\frac{1}{m} \sum_{i=1}^m y_i^2}} \quad (31)$$

2) *Probabilistic Forecast Metrics*: Probabilistic metrics evaluate the quality of the predicted *intervals* and the *full distribution*, assessing both sharpness (the width of the interval) and reliability (the coverage).
• **Prediction Interval Coverage Probability (PICP)**: measures the percentage of true values that fall within the model’s predicted interval. Let the prediction interval at time step i be defined by its lower and upper quantiles, $L_i = q_{\underline{\alpha}}^i$ and $U_i = q_{\overline{\alpha}}^i$, corresponding to a nominal confidence level $\gamma = 1 - \alpha$. For example, an 80% prediction interval corresponds to $\gamma = 0.8$ and $\alpha = 0.2$. We define the coverage indicator as follows:

$$c_i = \begin{cases} 1, & \text{if } y_i \in [L_i, U_i], \\ 0, & \text{otherwise.} \end{cases} \quad (32)$$

The PICP is then computed as follows:

$$\text{PICP} = \frac{100}{m} \sum_{i=1}^m c_i. \quad (33)$$

Ideally, PICP should be close to the nominal value 100γ , indicating well-calibrated predictive intervals.

• **Continuous Ranked Probability Score (CRPS)**: evaluates the quality of the entire predictive distribution by measuring the discrepancy between the predictive CDF F and the observed value y as shown below:

$$\text{CRPS}(F, y) = \int_{-\infty}^{\infty} (F(z) - \mathbf{1}\{y \leq z\})^2 dz, \quad (34)$$

where $\mathbf{1}\{\cdot\}$ denotes the indicator function. When only predictive samples $X^{(1)}, \dots, X^{(S)} \sim F$ are available, we approximate F using the empirical CDF, i.e.,

$$\hat{F}(z) = \frac{1}{S} \sum_{s=1}^S \mathbf{1}\{X^{(s)} \leq z\} \quad (35)$$

and compute CRPS at each time step accordingly [58].

B. Considered Baselines

To validate the performance of EMFusion, we conduct a comparative analysis against a suite of forecasting models. A brief description of each baseline model is provided below:

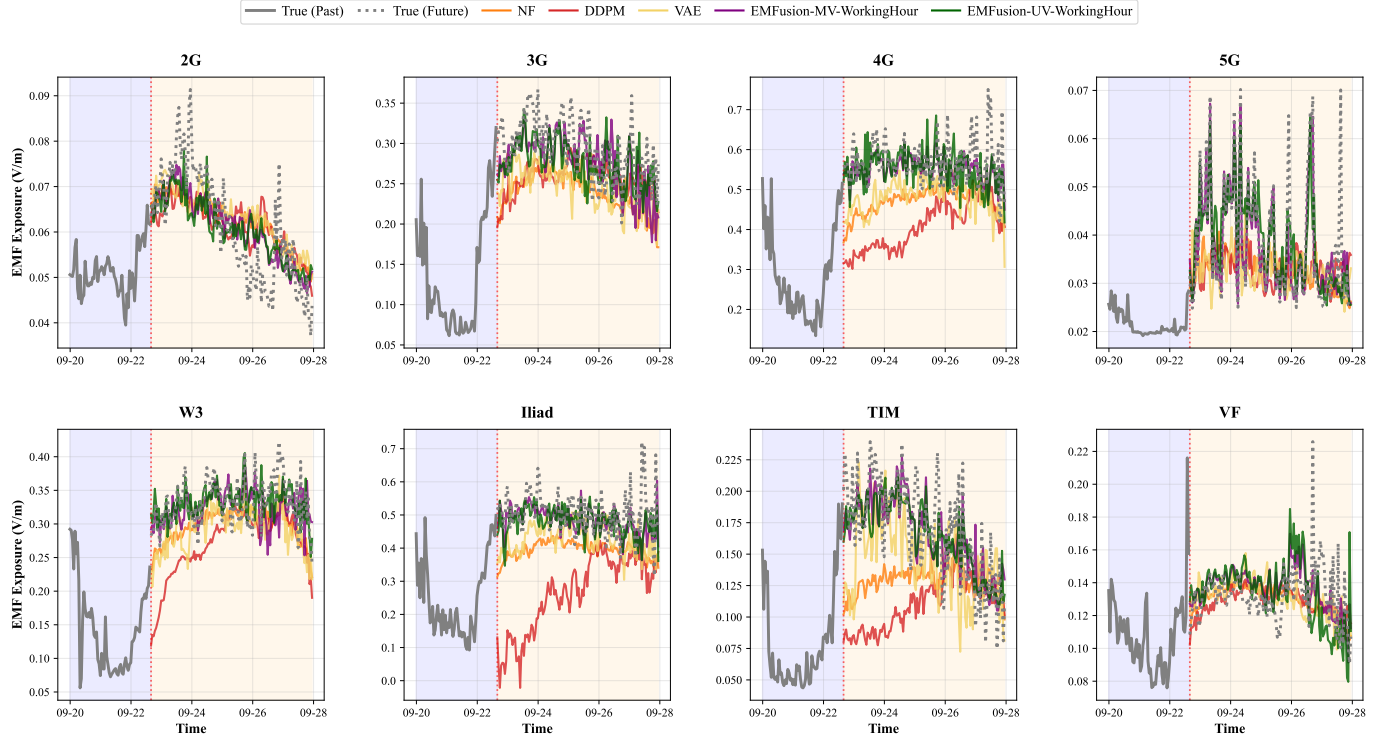


Fig. 6: Comparison of EMF Forecasts in Validation Set Across Technology Bands (Top) and Operators (Bottom)

- **DDPM** [59]: the model uses a U-Net denoiser with time-dependent noise embeddings and is trained to match the true forward diffusion process via noise-prediction.
- **WGAN** [5]: the generator maps historical EMF trajectories and latent noise to future EMF scenarios, while the critic enforces distributional realism through the Wasserstein loss with gradient penalty.
- **VAE** [60]: the encoder maps historical EMF sequences into a low-dimensional latent space, and the decoder reconstructs future EMF trajectories from sampled latent variables conditioned on the history. This yields a parametric predictive distribution via the latent Gaussian prior.
- **Normalizing Flow (NF)** [59]: Starting from a base distribution (e.g., multivariate Gaussian), a sequence of invertible transformations is learned to model the joint distribution of future EMF values given the past values, enabling exact likelihood evaluation and sampling.
- **Improved Quantile LSTM (IQLSTM)**: follows [61], where an LSTM-based temporal encoder outputs multiple conditional quantiles of the future EMF distribution. The model is trained using a pinball (quantile) loss over a set of pre-defined quantile levels, providing a non-parametric representation of forecast uncertainty for each time step.
- **Dropout-based Probabilistic Model**: Following the Monte Carlo Dropout approach of Gal and Ghahramani [62], this algorithm employs a deep LSTM forecaster with dropout layers activated both during training and inference, by running multiple stochastic forward passes with different dropout masks
- **TimeGrad**: TimeGrad [58] is a diffusion-based time-

series forecasting model that combines an autoregressive RNN backbone with a conditional diffusion head.

C. Evaluation Settings

All models were trained using an identical training dataset. Their respective hyperparameters were optimized via a grid search procedure on the validation datasets. All algorithms were executed using PyTorch on the Trillium high-performance computing cluster, hosted by SciNet at the University of Toronto. Specifically, we utilized the GPU-accelerated nodes, which are equipped with an AMD EPYC 9654 (Zen 4) 2.4 GHz CPU, 749 GB of system RAM, and four NVIDIA H100 SXM GPUs (80 GB memory each).

For each day, the EMF time series contains 192 regularly sampled observations. We use a 7-day lookback window, randomly sampled from the dataset, to predict the subsequent day. Formally, the historical input window is $H = 7 \times 192 = 1344$ time steps and the prediction window is $F = 192$ steps. During sampling, we generate $\hat{N} = 100$ scenarios for probabilistic forecasting. The hyperparameters for the EMFusion are set as follows: For training, the learning rate is $5e-4$, the batch size is 64, and the model is trained for 1500 epochs. The U-Net model has a depth of 6, and the attention mechanism uses 8 heads. In the simulations, physical constants include the free-space wave impedance $Z_0 = 376.73 \Omega$ and the antenna-gain calibration constant $A_{GC} = 9.73$.

D. Performance Evaluation

1) *Comparative Analysis of EMFusion without External Conditions*: **Table-III** analyzes the univariate forecasting per-

TABLE IV: A comparative analysis of univariate forecasting performance of EMFusion with imputation without external conditions. Metrics are ordered as CRPS, ND, NRMSE, MAPE, and PICP. Lower is better for CRPS, ND, NRMSE, MAPE; higher is better for PICP. **Bold** = best in row; underline = second best in row.

		Univariate					Multivariate				
Metric		EMFusion (Uncond.)	EMFusion (Seasons)	EMFusion (Workingday)	EMFusion (WorkingHour)	EMFusion (multi)	EMFusion (Uncond.)	EMFusion (Seasons)	EMFusion (Workingday)	EMFusion (WorkingHour)	EMFusion (multi)
W3	CRPS	0.0099	0.0111	0.0103	0.0097	0.0193	0.1096	0.1095	0.1091	0.0086	0.0365
	ND	<u>0.1108</u>	0.1265	0.1230	0.1156	0.2179	0.8993	0.8950	0.8935	0.0946	0.3300
	NRMSE	0.1601	0.1708	0.1715	0.1669	0.2673	0.9086	0.9041	0.9028	0.1467	0.3960
	MAPE	<u>11.79</u>	14.13	13.77	12.60	25.30	88.29	87.87	87.69	9.89	38.06
	PICP	50.49	48.91	<u>54.78</u>	60.26	43.41	0.00	0.00	0.00	52.69	24.88
Iliad	CRPS	0.0164	0.0173	0.0167	<u>0.0153</u>	0.0273	0.0724	0.0724	0.0680	0.0120	0.0435
	ND	0.1215	0.1334	0.1319	<u>0.1211</u>	0.1975	0.4382	0.4382	0.4041	0.0903	0.2759
	NRMSE	0.1744	0.1744	0.1795	<u>0.1724</u>	0.2380	0.4819	0.4819	0.4419	0.1469	0.3348
	MAPE	14.05	15.94	15.05	<u>13.93</u>	26.39	40.38	40.38	38.15	10.40	31.89
	PICP	50.15	52.66	53.51	56.40	39.08	11.37	11.37	10.76	63.02	27.86
TIM	CRPS	0.0066	0.0072	0.0066	0.0063	0.0122	0.0475	0.0475	0.0482	<u>0.0065</u>	0.0215
	ND	<u>0.1381</u>	0.1548	0.1522	0.1466	0.2572	0.7524	0.7524	0.7579	0.1374	0.3891
	NRMSE	0.2094	0.2180	0.2254	0.2184	0.3219	0.7756	0.7756	0.7810	0.2126	0.4356
	MAPE	<u>13.73</u>	16.20	15.91	15.02	25.63	72.80	72.80	73.31	<u>13.81</u>	43.49
	PICP	57.05	51.81	<u>57.11</u>	57.68	39.58	0.03	0.03	0.00	54.97	25.31
VF	CRPS	<u>0.0043</u>	0.0046	0.0044	<u>0.0043</u>	0.0077	0.0349	0.0349	0.0331	0.0036	0.0122
	ND	<u>0.1005</u>	0.1118	0.1078	0.1043	0.1806	0.6308	0.6308	0.6061	0.0826	0.2498
	NRMSE	<u>0.1762</u>	0.1878	0.1872	0.1862	0.2445	0.6438	0.6438	0.6210	0.1571	0.3039
	MAPE	<u>11.46</u>	12.35	12.15	11.74	19.34	62.48	62.48	59.82	9.67	25.23
	PICP	51.04	54.16	55.79	58.90	44.61	0.13	0.13	0.16	<u>56.56</u>	29.63
2G	CRPS	0.0070	0.0076	0.0071	0.0068	0.0131	0.0640	0.0639	0.0635	0.0062	0.0234
	ND	<u>0.1165</u>	0.1310	0.1276	0.1222	0.2186	0.7609	0.7594	0.7525	0.1049	0.2922
	NRMSE	<u>0.1819</u>	0.1922	0.1947	0.1905	0.2779	0.7760	0.7745	0.7683	0.1721	0.3542
	MAPE	<u>12.33</u>	14.22	13.94	13.12	23.42	74.52	74.38	73.61	11.13	29.57
	PICP	52.86	51.62	<u>55.90</u>	58.95	42.53	0.05	0.05	0.05	54.74	29.04
3G	CRPS	0.0093	0.0101	0.0095	<u>0.0089</u>	0.0166	0.0661	0.0661	0.0646	0.0077	0.0288
	ND	<u>0.1178</u>	0.1316	0.1287	0.1219	0.2133	0.6802	0.6791	0.6654	0.1012	0.3200
	NRMSE	<u>0.1800</u>	0.1877	0.1909	0.1860	0.2679	0.7025	0.7013	0.6867	0.1658	0.3805
	MAPE	<u>12.76</u>	14.65	14.22	13.32	24.17	65.99	65.88	64.74	10.95	38.29
	PICP	52.18	51.88	55.30	58.31	41.67	2.88	2.88	2.73	<u>56.81</u>	30.09
4G	CRPS	0.0090	0.0097	0.0092	<u>0.0086</u>	0.0162	0.0670	0.0669	0.0655	0.0074	0.0274
	ND	<u>0.1160</u>	0.1298	0.1268	0.1202	0.2113	0.6923	0.6911	0.6775	0.0994	0.2959
	NRMSE	<u>0.1783</u>	0.1865	0.1893	0.1847	0.2662	0.7130	0.7117	0.6974	0.1638	0.3536
	MAPE	<u>12.59</u>	14.45	14.04	13.16	23.90	67.33	67.21	66.03	10.78	32.58
	PICP	51.98	51.83	55.30	58.49	42.01	2.48	2.48	2.35	<u>56.50</u>	28.18
5G	CRPS	0.0085	0.0091	0.0086	<u>0.0081</u>	0.0149	0.0505	0.0505	0.0494	0.0071	0.0241
	ND	<u>0.1246</u>	0.1387	0.1360	0.1296	0.2231	0.6435	0.6435	0.6315	0.1119	0.3413
	NRMSE	<u>0.1923</u>	0.1995	0.2044	0.1989	0.2816	0.6692	0.6692	0.6562	0.1823	0.3899
	MAPE	<u>13.24</u>	15.17	14.76	13.93	24.25	62.11	62.11	61.15	11.93	39.23
	PICP	53.82	52.61	55.88	57.67	40.72	2.89	2.89	2.73	<u>57.38</u>	25.59

formance of the EMFusion model, configured with imputation and without external conditions. We compare it against several baselines, including generative models (NF, DDPM, VAE, WGAN) and other probabilistic forecasting models (IQLSTM, LSTM-Dropout). The evaluation is based on five key metrics, CRPS, ND, NRMSE, and MAPE (where lower is better) and PICP (where higher is better).

In both the operator-wise and technology-band-wise breakdowns, EMFusion consistently achieves the best scores for CRPS, ND, NRMSE, and MAPE, while only WGAN achieves a fractionally better NRMSE for the VF dataset. From the operator perspective, the performance gap is even more pronounced. EMFusion's CRPS (0.0067) and MAPE (14.18%) are far superior to all baselines in terms of TIM. We also observe EMFusion drastically reduces all error metrics in the 2G 3G and 4G dataset. While 5G dataset appears to be the most challenging, with higher error values for all models. Despite this, EMFusion still delivers the best performance in CRPS (0.0019), ND (0.1518), and MAPE (11.57%).

In terms of evaluation, the highest PICP scores are consistently achieved by DDPM and NF. For example, DDPM achieves an exceptional 90.22% for VF and 82.02% for 2G, while NF scores 72.44% for W3. This indicates that these models enable larger percentage of the true (observed) values

fall inside the model's prediction intervals. EMFusion provides a more balanced result, with PICP scores generally in the 50-60% range. This suggests it produces tighter, more accurate prediction intervals that are less conservative but more closely reflect the actual forecast.

Fig. 6 highlights the performance of multivariate EMFusion across all datasets organized by cellular technology bands and operators. Multivariate EMFusion with working hour condition provides the closest match to the ground truth EMF values, i.e., it reproduces the daily exposure cycle, aligns well with the timing of peaks and troughs, and preserves the moderate intra-day variability without following high-frequency noise. Univariate EMFusion with working hour condition exhibits a similar pattern but tends to slightly underestimate the most pronounced peaks in some panels. In contrast, NF and VAE generally produce smoother forecasts that track the overall trend but miss sharp local excursions, leading to significant phase and amplitude mismatches. DDPM is more responsive to transient fluctuations, but this often manifests as spurious oscillations and overfitting to local noise, especially in higher-exposure bands such as 4G and 5G.

2) *Univariate vs Multivariate Conditional EMFusion:* Table-IV shows the significance of incorporating appropriate contextual conditions in the reverse diffusion process. In

TABLE V: **Performance comparison** Lower is better for CRPS, ND, NRMSE, MAE, MAPE, and Energy Score; for PICP, a value closest to 80% is preferred. Best per column in **bold**. Reported as mean \pm standard error.

Method	CRPS	ND	NRMSE	MAE	MAPE	PICP	Energy Score
NF	0.0110 \pm 0.0070	0.1739 \pm 0.0332	0.2447 \pm 0.0941	0.0337 \pm 0.0219	18.1875 \pm 2.8910	69.1871 \pm 6.0702	0.0163 \pm 0.0103
IQLSTM	0.0120 \pm 0.0076	0.1829 \pm 0.0338	0.2575 \pm 0.0954	0.0351 \pm 0.0226	19.2144 \pm 2.6370	61.8676 \pm 5.9028	0.0192 \pm 0.0120
WGAN	0.0123 \pm 0.0071	0.1959 \pm 0.0507	0.2588 \pm 0.0999	0.0356 \pm 0.0210	21.3099 \pm 4.3154	50.0930 \pm 9.8127	0.0202 \pm 0.0114
VAE	0.0128 \pm 0.0083	0.1908 \pm 0.0411	0.2597 \pm 0.0971	0.0367 \pm 0.0237	20.6526 \pm 3.8411	52.2893 \pm 4.4282	0.0213 \pm 0.0139
DDPM	0.0132 \pm 0.0085	0.1989 \pm 0.0520	0.2647 \pm 0.0985	0.0385 \pm 0.0260	22.5219 \pm 6.0977	85.9521 \pm 6.4352	0.0156 \pm 0.0108
Dropout	0.0179 \pm 0.0117	0.2418 \pm 0.0481	0.2937 \pm 0.0867	0.0470 \pm 0.0299	30.2881 \pm 6.8275	27.9310 \pm 6.7606	0.0328 \pm 0.0218
EMFusion-Uncond.	0.0212 \pm 0.0154	0.2486 \pm 0.0688	0.3257 \pm 0.1048	0.0523 \pm 0.0377	23.6121 \pm 6.2094	33.0397 \pm 10.4381	0.0389 \pm 0.0284
EMFusion-MV(Multi)	0.0154 \pm 0.0102	0.2083 \pm 0.0412	0.2808 \pm 0.0955	0.0411 \pm 0.0266	22.8826 \pm 5.1239	41.6521 \pm 6.5349	0.0275 \pm 0.0185
EMFusion-MV(Working Day)	0.0696 \pm 0.0634	0.6345 \pm 0.2315	0.6705 \pm 0.2088	0.1433 \pm 0.1262	62.0675 \pm 22.9755	4.8629 \pm 7.7988	0.1381 \pm 0.1270
EMFusion-MV(Season)	0.0700 \pm 0.0635	0.6355 \pm 0.2347	0.6735 \pm 0.2123	0.1445 \pm 0.1265	61.9106 \pm 23.5813	5.7850 \pm 8.1614	0.1388 \pm 0.1272
EMFusion-MV(WorkingHour)	0.0071 \pm 0.0043	0.1049 \pm 0.0241	0.1858 \pm 0.0936	0.0195 \pm 0.0120	10.7561 \pm 1.4898	56.4799 \pm 5.0838	0.0118 \pm 0.0072

particular, the **WorkingHour**-conditioned EMFusion achieves the lowest CRPS, ND, NRMSE, and MAPE regardless of the operator (W3, Iliad, TIM, VF) or technology band (2G–5G). The multi-conditioned multivariate model (last column) does not surpass the **WorkingHour**-only model, suggesting that fine-grained time-of-day conditioning captures most of the useful temporal structure for EMF exposure, while additional context yields diminishing returns. From the operator perspective, TIM and VF benefit strongly from conditional diffusion: for example, under multivariate modeling their CRPS and MAPE values under EMFusion (WorkingHour) are an order of magnitude smaller than unconditioned EMFusion, indicating substantially sharper and more accurate forecasts.

From the technology-band viewpoint, EMFusion sharply reduces all error metrics for legacy bands (2G, 3G, 4G), with the largest relative gains observed for 4G, where EMFusion (WorkingHour) approximately halves the CRPS and MAPE compared to unconditioned EMFusion in the multivariate setting. The 5G band remains the most challenging case, with uniformly higher errors across all models due to its more volatile traffic and deployment patterns. Nonetheless, EMFusion still delivers the best multivariate performance in CRPS, ND, and MAPE for 5G, indicating that the diffusion-based approach remains robust even under rapidly fluctuating EMF dynamics. In terms of interval quality, unconditioned EMFusion exhibits very low PICP values in the multivariate case, reflecting overly narrow and under-dispersed prediction intervals. EMFusion, by contrast, achieves PICP values predominantly in the 50–65% range across operators and bands, with the **WorkingHour** configuration again performing best. Although these values are below the ideal 80% target, they indicate tighter, less conservative intervals that are more informative than those from unconditioned EMFusion.

Table V reports the forecasting performance of all methods, averaged over all carriers and technologies. The proposed **EMFusion-MV-WorkingHour** consistently outperforms across all error- and distribution-based scores, indicating sharper and better-calibrated predictive distributions. Although its PICP is slightly lower than that of DDPM, it remains competitive with the strongest baselines while delivering substantially improved overall forecasting quality.

VI. CONCLUSION

Existing EMF forecasting approaches do not fully exploit the spatio-temporal dependencies across multiple frequency bands, operators, and contextual conditions. This study introduced EMFusion, a conditional diffusion based probabilistic forecasting framework. The framework employs conditional embeddings, cross-attention based context integration, and imputation-based sampling to improve temporal coherence. Experiments on real EMF datasets showed that EMFusion achieved lower deterministic forecasting errors and better probabilistic calibration than representative deep learning time-series and generative baselines across different operators and frequency selections, and that the predicted point values and prediction intervals were closer to the observed EMF trajectories. Future work may incorporate base-station location, transmit power, user distribution, and reconfigurable intelligent surface deployments as additional conditioning variables to further tighten the forecast distribution.

ACKNOWLEDGMENT

The authors would like to thank Daniele Franci and Settimio Pavoncello for providing the EMF measurement hardware used to collect the Italian dataset.

REFERENCES

- [1] X. Mootoo, H. Tabassum, and L. Chiaravliglio, “EMForecaster: A deep learning framework for time series forecasting in wireless networks with distribution-free uncertainty quantification,” *IEEE Trans. on Netw. Science and Eng.*, vol. 13, pp. 1207–1225, 2026.
- [2] L. Chiaravliglio, A. Elzanaty, and M.-S. Alouini, “Health risks associated with 5G exposure: A view from the communications engineering perspective,” *IEEE Open J. Commun. Soc.*, vol. 2, pp. 2131–2179, 2021.
- [3] International Commission on Non-Ionizing Radiation Protection (ICNIRP), *Guidelines for limiting exposure to electromagnetic fields (100 kHz to 300 GHz)*, 2020, actual citation for ICNIRP 2020 guidelines.
- [4] R. Stam, “Comparison of international policies on electromagnetic fields: (power frequency and radiofrequency fields),” National Institute for Public Health and the Environment (RIVM), Netherlands, Tech. Rep., 2018, placeholder for a general EMF policy comparison report.
- [5] Y. Huang, J. Pei, L. Chen, Z. Du, J. Chen, and Z. Peng, “Probabilistic Net Load Forecasting for High-Penetration RES Grids Utilizing Enhanced Conditional Diffusion Model,” *arXiv preprint arXiv:2503.17770*, 2025.
- [6] J. Sohl-Dickstein, E. Weiss, N. Maheswaranathan, and S. Ganguli, “Deep unsupervised learning using nonequilibrium thermodynamics,” in *Proc. Int. Conf. Mach. Learn.* pmlr, 2015, pp. 2256–2265.
- [7] J. Ho, A. Jain, and P. Abbeel, “Denoising diffusion probabilistic models,” in *Adv. Neural Inf. Process. Syst.*, vol. 33, 2020, pp. 6840–6851.

[8] J. Pei, J. Wang, D. Shi, and P. Wang, "Detection and imputation based two-stage denoising diffusion power system measurement recovery under cyber-physical uncertainties," *IEEE Trans. Smart Grid*, vol. 15, no. 6, pp. 5965–5980, Nov. 2024.

[9] J. Pei, C. Feng, P. Wang, H. Tabassum, and D. Shi, "Latent diffusion model-enabled low-latency semantic communication in the presence of semantic ambiguities and wireless channel noises," *IEEE Trans. Wireless Commun.*, vol. 24, no. 5, pp. 4055–4072, May 2025.

[10] A. Borovykh, S. Bohte, and C. W. Oosterlee, "Conditional time series forecasting with convolutional neural networks," *arXiv preprint arXiv:1703.04691*, 2017.

[11] A. Y. Nikravesh, S. A. Ajila, C.-H. Lung, and W. Ding, "Mobile network traffic prediction using MLP, MLPWD, and SVM," in *Proc. IEEE Int. Congr. Big Data (BigData Congress)*. IEEE, 2016, pp. 402–409.

[12] M. Di Mauro, G. Galatò, F. Postiglione, W. Song, and A. Liotta, "Multivariate time series characterization and forecasting of VoIP traffic in real mobile networks," *IEEE Trans. on Netw. and Service Manage.*, vol. 21, no. 1, pp. 851–865, 2023.

[13] A. Dalgkitis, M. Louta, and G. T. Karetos, "Traffic forecasting in cellular networks using the LSTM RNN," in *Proc. of the 22nd Pan-Hellenic conference on informatics*, 2018, pp. 28–33.

[14] M. A. Habib, P. E. I. Rivera, Y. Ozean, M. Elsayed, M. Bavand, R. Gaigalas, and M. Erol-Kantarci, "Transformer-based wireless traffic prediction and network optimization in o-ran," in *Proc. IEEE Int. Conf. Commun. Wkshps. (ICC Wkshps.)*. IEEE, 2024, pp. 1–6.

[15] C. Fiandrino, E. P. Gómez, P. F. Pérez, H. Mohammadalizadeh, M. Fiore, and J. Widmer, "AIChronoLens: advancing explainability for time series AI forecasting in mobile networks," in *Proc. IEEE Int. Conf. Comput. Commun. (INFOCOM)*. IEEE, 2024, pp. 1521–1530.

[16] D. P. Isravel, S. Silas, J. W. Kathrine, E. B. Rajsingh, and J. Andrew, "Multivariate forecasting of network traffic in SDN-based ubiquitous healthcare system," *IEEE Open J. of the Commun. Soc.*, vol. 5, pp. 1537–1550, 2024.

[17] S. P. Sone, J. J. Lehtomäki, and Z. Khan, "Wireless traffic usage forecasting using real enterprise network data: Analysis and methods," *IEEE Open J. of the Commun. Soc.*, vol. 1, pp. 777–797, 2020.

[18] Y. Zhang, Y. Wu, A. Liu, X. Xia, T. Pan, and X. Liu, "Deep learning-based channel prediction for LEO satellite massive MIMO communication system," *IEEE Wireless Commun. Lett.*, vol. 10, no. 8, pp. 1835–1839, 2021.

[19] A. Hameed, J. Violos, A. Leivadeas, N. Santi, R. Grünblatt, and N. Mitton, "Toward QoS prediction based on temporal transformers for IoT applications," *IEEE Trans. on Netw. and Service Manage.*, vol. 19, no. 4, pp. 4010–4027, 2022.

[20] H. E. Dinaki, S. Shirmohammadi, E. Janulewicz, and D. Côté, "Forecasting video QoE with deep learning from multivariate time-series," *IEEE Open J. of Signal Process.*, vol. 2, pp. 512–521, 2021.

[21] A. G. Colpitts and B. R. Petersen, "Short-term multivariate KPI forecasting in rural fixed wireless LTE networks," *IEEE Netw. Lett.*, vol. 5, no. 1, pp. 11–15, 2023.

[22] E. Zhang, Z. Liu, Y. Xiang, and Y. Qu, "Probabilistic QoS metric forecasting in delay-tolerant networks using conditional diffusion models on latent dynamics," *arXiv preprint arXiv:2504.08821*, 2025.

[23] Y. Kiouvrekis, I. Givisis, T. Panagiotakopoulos, I. Tsilikas, A. Ploussi, E. Spyratou, and E. P. Efstatopoulos, "A comparative analysis of explainable artificial intelligence models for electric field strength prediction over eight european cities," *Sensors*, vol. 25, no. 1, p. 53, 2024.

[24] M. R. Bakcan *et al.*, "Measurement and prediction of electromagnetic radiation exposure level in a university campus," *Tehnički vjesnik*, vol. 29, no. 2, pp. 449–455, 2022.

[25] Z. Pala, "Examining EMF time series using prediction algorithms with R," *IEEE Can. J. Elect. Comput. Eng.*, vol. 44, no. 2, pp. 223–227, 2021.

[26] C. Nguyen, A. A. Cheema, C. Kurnaz, A. Rahimian, C. Brennan, and T. Q. Duong, "Deep learning models for time-series forecasting of RF-EMF in wireless networks," *IEEE Open J. of Commun. Soc.*, vol. 5, pp. 1399–1414, 2024.

[27] G. E. P. Box, G. M. Jenkins, G. C. Reinsel, and G. M. Ljung, *Time Series Analysis: Forecasting and Control*, 5th ed. Hoboken, NJ: John Wiley & Sons, 2015.

[28] P. De Lellis, F. L. Iudice, and N. Pasquino, "Time-series-based model and validation for prediction of exposure to wideband radio frequency electromagnetic radiation," *IEEE Trans. Instrum. Meas.*, vol. 69, no. 6, pp. 3198–3205, 2019.

[29] A. Al-Jumaily, A. Sali, M. Riyadh, S. Q. Wali, L. Li, and A. F. Osman, "Machine learning modeling for radiofrequency electromagnetic fields (RF-EMF) signals from mmWave 5G signals," *IEEE Access*, vol. 11, pp. 79 648–79 658, 2023.

[30] Y. Li, X. Lu, Y. Wang, and D. Dou, "Generative time series forecasting with diffusion, denoise, and disentanglement," *Adv. Neural Inf. Process. Syst.*, vol. 35, pp. 23 009–23 022, 2022.

[31] I. J. Goodfellow, J. Pouget-Abadie, M. Mirza, B. Xu, D. Warde-Farley, S. Ozair, A. Courville, and Y. Bengio, "Generative adversarial nets," *Adv. Neural Inf. Process. Syst.*, vol. 27, 2014.

[32] A. Koochali, A. Dengel, and S. Ahmed, "If you like it, gan it—probabilistic multivariate times series forecast with gan," *Eng. Proc.*, vol. 5, no. 1, p. 40, 2021.

[33] Y. Song and S. Ermon, "Generative modeling by estimating gradients of the data distribution," in *Adv. Neural Inf. Process. Syst.*, vol. 32, 2019.

[34] K. Rasul, C. Seward, I. Schuster, and R. Vollgraf, "Autoregressive denoising diffusion models for multivariate probabilistic time series forecasting," in *Proc. Int. Conf. Mach. Learn. (PMLR)*, 2021, pp. 8857–8868.

[35] Y. Tashiro, J. Song, Y. Song, and S. Ermon, "CSDI: Conditional Score-based Diffusion Models for Probabilistic Time Series Imputation," in *Adv. Neural Inf. Process. Syst.*, vol. 34, 2021, pp. 24 804–24 816.

[36] J. M. L. Alcaraz and N. Strodthoff, "Diffusion-based time series imputation and forecasting with structured state space models," *arXiv preprint arXiv:2208.09399*, 2022.

[37] Z. Yan, J. Pei, H. Wu, H. Tabassum, and P. Wang, "Semantic-aware adaptive video streaming using latent diffusion models for wireless networks," *IEEE Wireless Commun.*, vol. 32, no. 5, pp. 30–38, 2025.

[38] M. Kollovieh, A. F. Ansari, M. Bohlke-Schneider, J. Zschiegner, H. Wang, and Y. B. Wang, "Predict, refine, synthesize: Self-guiding diffusion models for probabilistic time series forecasting," *Adv. Neural Inf. Process. Syst.*, vol. 36, pp. 28 341–28 364, 2023.

[39] X. Yuan and Y. Qiao, "Diffusion-ts: Interpretable diffusion for general time series generation," *arXiv preprint arXiv:2403.01742*, 2024.

[40] J. Liu, L. Yang, H. Li, and S. Hong, "Retrieval-augmented diffusion models for time series forecasting," *Adv. Neural Inf. Process. Syst.*, vol. 37, pp. 2766–2786, 2024.

[41] L. Shen, W. Chen, and J. Kwok, "Multi-resolution diffusion models for time series forecasting," in *Proc. Int. Conf. Learn. Represent.*, 2024.

[42] Q. Li, Z. Zhang, L. Yao, Z. Li, T. Zhong, and Y. Zhang, "Diffusion-based decoupled deterministic and uncertain framework for probabilistic multivariate time series forecasting," in *Proc. Int. Conf. Learn. Represent.*, 2025.

[43] C. Meijer and L. Y. Chen, "The rise of diffusion models in time-series forecasting," *arXiv preprint arXiv:2401.03006*, 2024.

[44] C. Su, Z. Cai, Y. Tian, Z. Zheng, and Y. Song, "Diffusion Models for Time Series Forecasting: A Survey," *arXiv preprint arXiv:2507.14507*, 2025.

[45] J. Ho, A. Jain, and P. Abbeel, "Denoising Diffusion Probabilistic Models," in *Adv. Neural Inf. Process. Syst.*, vol. 33, 2020.

[46] J. Ho and T. Salimans, "Classifier-free diffusion guidance," in *Proc. NeurIPS 2021 Workshop on Deep Generative Models and Downstream Appl.*, 2021. [Online]. Available: <https://openreview.net/forum?id=qw8AKxfYbI>

[47] Keysight Technologies. (2025) N6850A broadband omnidirectional antenna. Keysight Technologies. Product page. [Online]. Available: <https://www.keysight.com/ca/en/product/N6850A/broadband-omnidirectional-antenna.html>

[48] O. Ronneberger, P. Fischer, and T. Brox, "U-net: Convolutional networks for biomedical image segmentation," in *Proc. Int. Conf. Med. Image Comput. Comput.-Assist. Interv. (MICCAI)*. Springer, 2015, pp. 234–241.

[49] K. He, X. Zhang, S. Ren, and J. Sun, "Deep residual learning for image recognition," in *Proc. IEEE Conf. Comput. Vis. Pattern Recognit. (CVPR)*, 2016, pp. 770–778.

[50] A. Vaswani, N. Shazeer, N. Parmar, J. Uszkoreit, L. Jones, A. N. Gomez, L. Kaiser, and I. Polosukhin, "Attention Is All You Need," in *Adv. Neural Inf. Process. Syst.*, vol. 30, 2017, pp. 5998–6008.

[51] R. Rombach, A. Blattmann, D. Lorenz, P. Esser, and B. Ommer, "High-resolution image synthesis with latent diffusion models," in *Proc. IEEE Conf. Comput. Vis. Pattern Recognit. (CVPR)*, 2022, pp. 10 674–10 685.

[52] O. Petit, N. Thome, C. Rambour, L. Themyr, T. Collins, and L. Soler, "U-net transformer: Self and cross attention for medical image segmentation," in *Int. Workshop on Mach. Learn. in Medical Imaging*. Springer, 2021, pp. 267–276.

[53] L. Chiaraviglio, C. Lodovisi, D. Franci, S. Pavoncello, and T. Aureli, "Six months in the life of a cellular tower: Is 5G exposure higher than pre-5G one?" in *Proc. IEEE Int. Symp. Meas. Netw.* IEEE, 2022, pp. 1–6.

- [54] Anritsu Company. (2022) Remote spectrum monitor MS27102A. Anritsu Company. Product page. [Online]. Available: <https://www.anritsu.com/en-us/test-measurement/products/ms27102a>
- [55] ARPA Lazio. (2017) SearcH24 — software for remote control of non-vector spectrum analyzers. ARPA Lazio. AIRP 2017 proceedings. [Online]. Available: https://www.airp-asso.it/wp-content/uploads/convegni/2017_Salerno/Atti%20Salerno%202017.pdf
- [56] Keysight Technologies, “Antenna factor N6850A,” <https://www.keysight.com/main/redirector.jspx?action=ref&ckey=3104458&cname=EDITORIAL>, 2025, excel data file.
- [57] Università degli Studi di Roma “Tor Vergata”. (2025, 3) Academic Calendar 2024–2025. Accessed 2025-07-27. [Online]. Available: <https://web.uniroma2.it/en/contenuto/academic-calendar>
- [58] K. Rasul, C. Seward, I. Schuster, and R. Vollgraf, “Autoregressive Denoising Diffusion Models for Multivariate Probabilistic Time Series Forecasting,” in *Proc. Int. Conf. Mach. Learn.*, vol. 139. PMLR, 2021. [Online]. Available: <https://proceedings.mlr.press/v139/rasul21a.html>
- [59] E. H. Capel and J. Dumas, “Denoising diffusion probabilistic models for probabilistic energy forecasting,” in *Proc. IEEE Belgrade PowerTech*, Belgrade, Serbia, 2023, pp. 1–6.
- [60] S. R. Khazeiynasab, R. Iyengar, and W. L. Leow, “Probabilistic individual short-term load forecasting using conditional variational autoencoder,” in *Proc. IEEE Power Energy Soc. Gen. Meet. (PESGM)*, Orlando, FL, USA, 2023, pp. 1–5.
- [61] Q. Huang and S. Wei, “Improved quantile convolutional neural network with two-stage training for daily-ahead probabilistic forecasting of photovoltaic power,” *Energy Conv. Manag.*, vol. 220, p. 113085, Sep. 2020.
- [62] Y. Gal and Z. Ghahramani, “Dropout as a bayesian approximation: Representing model uncertainty in deep learning,” in *Proc. Int. Conf. Mach. Learn.*, vol. 48, 2016, pp. 1050–1059.